Automation in Construction 187 (2026) 106952

Contents lists available at ScienceDirect

Automation in Construction

journal homepage: www.elsevier.com/locate/autcon

Comparative evaluation of robotically assembled discrete lattice systems for sustainable construction

Miana Smith [a], Paul Richard [b], Alfonso Parra Rubio [a], Neil Gershenfeld [a]

[a] Center for Bits and Atoms, MIT, 75 Amherst Street, Cambridge, 02142, MA, USA
[b] School of Engineering, École Polytechnique Fédérale de Lausanne, 1015 Rte Cantonale, Lausanne, Switzerland

ARTICLE INFO

Keywords:
Robotic assembly
Architected lattices
Sustainability
Construction automation
Distributed robotics
Modular building systems
Additive manufacturing

ABSTRACT

Additive manufacturing could improve the sustainability and efficiency of building construction, but current methods fall short. Continuous methods, such as 3-D printing, face challenges in error-correction, structural integrity, and accessible build volume, while assembly-based approaches typically require high mechanical precision, leading to costly and complex machines or off-site fabrication. This paper proposes robotically assembled discrete architected lattices, or voxels, as an in-situ construction method with low environmental impact and competitive speed and cost. Voxel-based structures can be scalably and incrementally assembled using distributed low-cost robots. The performance of multiple voxel types is compared against 3-D printed concrete, precast modular concrete, concrete masonry units, steel framing, and stick framing for a simplified 1-story building. The results indicate voxel-based systems can reduce embodied carbon by up to 76%–82% relative to 3-D printed concrete, with competitive cost and construction timelines, demonstrating the potential of distributed building-block assembly as a sustainable route to automated in-situ construction.

1. Introduction

The construction industry drives 38% of global greenhouse gas emissions in energy [1], a significant problem, especially since construction demand is projected to continue to increase [2]. Digital fabrication has been proposed as a potential approach to mitigate the environmental impacts of construction by enabling more material-efficient designs with more diverse materials [3], while also improving the overall efficiency of construction, which is currently low [4,5]. Although digital fabrication methods offer promise for improving the sustainability and efficiency of manufacturing in other fields, such as aerospace [6], they face additional challenges for building construction due to large structure sizes and variable building environments [7]. Managing the competing needs to balance precision and assembly throughput over large distances in relatively unstructured environments has led towards automation methods that are often large, complex, and expensive [8]. These systems rely on either very large machines, such as with concrete 3D printers [9], or repurposed industrial robot arms, such as in [10], to manage error accumulation, and handle heavy loads, but these fairly complex and inflexible automation systems introduce additional challenges that can inhibit broad adoption [8]. At the same time, while research in distributed robotic systems has demonstrated the ability to build large structures with relatively simple robots, many of these systems do not seriously consider how they might scale to practical real world building scenarios. In this work, we evaluate the feasibility of robotically assembled discrete lattices as an alternative approach to on-site building construction.

Our proposed approach is to use robotically assembled blocks of architected lattice material to form a material-efficient, robust, and automated building process for the structural elements of a building. Architected lattices are a method to achieve efficiently distributed mass in a given structure [11], similar to truss structures commonly used for the construction of bridges or space frames. To apply these systems beyond the micro- or macro-scale, a regular lattice can be decomposed into repeating unit cells, or voxels, which can then be assembled into much larger structures, maintaining the advantageous properties of the basic architected lattice geometry [12]. Recent work has demonstrated the robotic assembly of meter-scale load bearing voxel structures [13], while other recent work in [14] evaluated the use of voxels in a load-bearing wall versus other construction methods, demonstrating lower embodied emissions for the voxel approach. These results indicate potential promise toward using a voxel-based approach for building construction, where robotic voxel assembly could offer the following:

- Material efficiency and sustainability benefits due to voxel structural performance
- Reliable building tolerances through continuous error-correction during the incremental assembly process

Corresponding author.
E-mail address: miana@mit.edu (M. Smith).

https://doi.org/10.1016/j.autcon.2026.106952
Received 24 October 2025; Received in revised form 2 April 2026; Accepted 6 April 2026
Available online 23 April 2026

- Efficient scalability through increasing robot quantities
- Low capital costs as the co-design of the robots and voxels enables a simpler robotic system
- A future route to fully reconfigurable structures

In this work, we project the performance of voxel-based building strategies against existing construction methods for a simplified one-story building. Based on the existing literature, we evaluated the mechanical performance and sustainability of eight voxel types, and we also designed and manufactured a new set of three voxel types compatible with robotic assembly. Using these, we evaluated the throughput and cost of a mobile robotic assembly system in hardware, to determine realistic time and cost estimates for voxel-based construction approaches. We compare these results against the performance of 3D concrete printing, precast modular concrete, concrete masonry units, cold-formed steel framing, and stick framing, across three main metrics: embodied carbon, material and fabrication cost, and building time. From this comparative study, we find that voxel approaches have the potential to reduce greenhouse gas emissions, cost, and assembly speed compared to existing construction approaches; however, the choice of lattice type, manufacturing process, and base material is critical to achieve any potential benefits. Our primary contribution is the evaluation of the efficiency of a robotically assembled voxel building system for construction in terms of sustainability, cost, and speed.

2. Background

In this section, we discuss current popular approaches to automating large-scale fabrication. We cover continuous extrusion-based processes, such as concrete 3D printing, and assembly-based processes using both static machines and distributed robotics.

2.1. 3D printing systems

Of the continuous extrusion processes, 3D concrete printing, or 3DCP, currently commands the most research attention [15]. Multiple buildings have been demonstrated with this methodology, including multi-story buildings [16] and commercially available housing developments [17]. In a 3DCP system, a concrete mixture typically consisting of Portland cement and sand is extruded in layers, either through a gantry system or an industrial arm [7]. However, this approach faces many challenges. From a sustainability perspective, material savings promised by the freedom of additive manufacturing are often not realized or are minimal [18], and the composition of the concrete used is typically more carbon-intensive than traditional concrete [19]. Although some studies have shown that 3DCP buildings have lower embodied carbon values compared to standard reinforced concrete buildings [18,19], this is derived in large part from the lack of steel reinforcement, negatively affecting structural performance. Besides, this contrasts with the predominant commercial use of this technology, which uses the 3D printed structure primarily as a stay-in-place formwork for traditional reinforced concrete [20,21], which results in worse sustainability outcomes because of the inefficient use of material. Additionally, many concrete printing blends have higher embodied greenhouse gas emissions because of the higher cement and additive concrete blends needed for printability [14].

Beyond these issues, concrete structures cannot be non-destructively changed, such as running new utilities through a building or changing interior wall layouts, and the material cannot be meaningfully recycled [22]. Although concrete structures in general are often cited for their durability [23], due to challenges in material formulation and inter-layer bonding, these benefits may not fully extend to current 3DCP approaches [24]. And, though there is currently research on methods for reinforcing extruded concrete, such as [25], these still face significant challenges before deployment, which limits the application of 3-D printing primarily to compression-only components. Even then, it is common for 3DCP to simply be used as formwork for standard reinforced concrete [21], further lowering the value proposition of the system.

Due to these challenges, there is active work on printing with more sustainable materials, such as with earthen mixtures [22]. WASP, for example, has demonstrated multiple buildings printed using a locally produced earth mixture [26]. This work is still limited by the lack of reinforcement, resulting in materials-intensive buildings, which can negate some sustainability benefits [22]. Unlike standard concrete, these structures offer the potential for recycling the base building material, leading to a more circular lifespan [22].

Various other projects have explored printing beyond cementitious materials, such as plastics and metals. [27] has demonstrated a bio-based polymer single-story house for research purposes, while [28] has demonstrated multiple spanning pedestrian bridges made of thermoplastic. [29] has demonstrated off-site printed truss lattices for multiple architecture-scale pavilions, sculptures, and cladding. Additionally, [30] demonstrated a 3-D printed welded steel pedestrian bridge, and on a similar scale, 3-D printed metal rocket parts have been demonstrated [31]. In particular, in these projects, the fabrication of the structure is done off-site and later delivered to the site. This is done as the complete structure, in the case of [30], or as large modules, as in [28], which are then installed in situ. This represents a similar workflow to prefabricated modular building units, but without the benefits of mass-production [32].

2.2. Assembly-basedapproaches

Other large-scale construction platforms have explored assembly-based approaches. Bricklaying has been automated by multiple groups, such as [33], which uses a robot arm on a mobile base to place clay bricks, or [34], which uses a telescopic 32-meter robotic arm to place mortar-less concrete masonry units (CMUs). Timber frame assembly has been explored using mobile robots as well as fixed gantry style assembly, such as in [35,36], and has been commercially deployed by [37] for load-bearing framing. More uncommon material systems have also been demonstrated, such as filament winding in [38]. Although these projects avoid the challenges of concrete deposition, they are still limited by either the need for high human intervention, an extremely well-defined build area, or highly expensive machines. These limitations stem from the challenges of maintaining accuracy over building-scale sizes—that is, error in the placement of a single element, such as a brick, impacts future placements and compounds on any prior errors.

Across these approaches, there is additionally a clear challenge in scaling beyond one- to two-story buildings, in that the operating envelope of the building system limits the ultimate size of the assembled structure. Beyond simply building vertically, these approaches would also face challenges in any project with an overall large footprint, especially for buildings or structures in difficult to access areas that cannot support large machines, such as for infrastructure development [39]. This is especially true for gantry girder systems, which are typical of current commercial demonstrations of 3DCP. Though this issue can be partially mitigated by using an industrial arm on a mobile base, or by moving the anchoring of a gantry printer, this presents multiple challenges of path planning and re-indexing position [39], which has so far limited the performance of this type of system.

Prefabrication of larger modules also presents an opportunity to leverage digital fabrication or manufacturing processes on the construction site. Fully prefabricated housing modules, such as [40], have existed on the market for some time, but are limited in their ability to be customized and easily transported. Panel-based approaches alleviate many of these challenges, and are available in a range of material types and applications. Pre-cast modular concrete systems are relatively common for large commercial and industrial applications and in smaller projects that do not require a high degree of customization,

such as for basement foundations [41]. Other methods, such as tilt-up slabs [42] or stay-in-place insulated concrete formwork [43] also enable a form of overall increased automation. The size and weight of these concrete systems can make installation difficult, and can make attempts at automating these processes more difficult.

Wood-based modular systems are also common and avert some of the challenges of the modular concrete systems. These can span a wide range of finishes, complexities, and applications. At the simple end, structural insulated panels are common in residential construction [44], while many companies provide more finished panel systems as well. Some of these more directly leverage robotic control or digital fabrication in their production processes to enable easier customization [45]. Using digital fabrication processes during the production of these larger modular panels can additionally help enable future automation of their assembly. [46] for example, explores using material-integrated assembly features to enable automatic assembly via a heterogeneous robotic system toward high performance timber buildings. By moving the production of these systems on site in structured environments, these systems can further avoid challenges associated with transporting large structural elements (and designing them to survive transport). This can be achieved through the development of systems akin to microfactory modules [10].

Other approaches to automation on the construction site involve the direct automation of existing equipment or processes for robotic operation. These approaches often address specific subtasks of the construction project which potentially limits their ability to achieve full autonomous function [8]. Commercial examples of these types of systems include [47] for bulldozing, or robots for drywall hanging [48].

2.3. Distributed robotics

Distributed robotic construction systems have been demonstrated to build structures much larger than the individual assembler itself [49]. In a distributed robotic construction system, many mobile robots individually pick and place new material to build a structure, and thus avoid constraints on the building envelope. Although various aerial drone systems have been demonstrated, such as in [50] with foam bricks, [51] with cables, or [52] with specially-designed concrete masonry, these face additional challenges in path planning, coordination, and payload weight limits for flying systems. Alternatively, robots that locomote over or through the structure are also common, such as [53], where robots stack magnetic bricks, [54] where micro-robots assemble carbon fiber trusses, or [55], where robots stack wood framing. The performance of some of these systems may be improved by considering how they can operate in conjunction with larger robotic systems, as more multi-scale and heterogeneous robotic systems [46]. Examples of this include [56], which explores using a relative robot to lay continuous filament into larger wood panels toward the architectural scale, and [57] which explores using a robotic clamping system in conjunction with industrial robot arms for architecture scale assembly demos in a lab environment.

Though many distributed robotic construction systems have been demonstrated, most of these demonstrations are on a relatively small scale and have very limited mechanical performance. However, some systems have demonstrated the ability to support spanning structures. Specifically, [13,58] demonstrate robotically assembled voxel systems that are load-bearing. While [58] only demonstrates this for centimeter-scale objects, [13] demonstrates a meter-scale structure assembled by a 3-robot team over several days.

2.4. Architected lattices

Distributed robotic assembly of discrete elements faces an inherent challenge in terms of balancing unit count, resolution, and structural integrity against each other. While using smaller assembly units leads to better geometric resolution and lowered demands on the robotic assembly system, this leads to a larger amount of units needed for a given structure, and with that, a higher number of joints between units, which introduce further opportunities for assembly error and can reduce the overall strength and stiffness of the final structure. For this work, we explore using discretely assembled architected lattices because these systems are specifically designed around minimizing the impact of the joint systems on the overall structure's behavior.

Prior literature on architected lattices has established that these structures can achieve better stiffness and strength scaling at light weights [12], though much of this prior work has utilized micrometer to millimeter scale fabrication processes, such as two photon lithography [59], which limits the application of these types of structures. However, the behavior of these lattices is largely governed by their geometries, and so is relatively scale-agnostic. This means that physically larger versions of these lattices assembled from discrete components can achieve equivalent mechanical properties using scaled-up versions of the same geometries. This is demonstrated in [12], which used interlocking faces made from oriented carbon fiber to form a node-connected octet lattice with lattice pitch on the order of tens of millimeters. [12] demonstrated superior stiffness results in the ultra-lightweight regime compared to continuously manufactured microlattices. Similarly, [60] demonstrates comparable performance to hollow-tube metallic microlattices using injection molded fiber reinforced plastic voxels with a 75 millimeter lattice pitch. Prior work has demonstrated comparable or superior performance to continuously produced microlattices, such as the metallic and polymer microlattices described in [61] or [59], while spanning a range of unit cell sizes from 15 mm [62] to 300 mm [13]. These systems have been used to assemble structures on the single meter scale, such as bridges [63], furniture [64], aerostructures [65], or vehicles [66].

These macro-scale assembly-based architected lattices achieve equivalent behavior to their continuously manufacturing micro-scale counterparts because in both cases the overall behavior is dominated by the lattice geometry, and not by the connectors between the discrete components. This is achieved by carefully designing the connections such that they are very stiff relative the beam elements, while adding minimal weight, which can be achieved through a variety of connection types and materials through considering the overall load path. [12] for example, interleaves the structural face components to constrain all but one degree of freedom, with a secondarily installed clip acting as a shear constraint. [60] directly transmits loads through the connectors, but uses steel screws and nuts, which are substantially stiffer than the FRP beams, such that the overall behavior is dominated by the beam geometry. These joints are also typically designed with mechanical alignment features that enable a higher degree of alignment between components, such as the quasi-kinematic surface features from [60,63], or [13]. Larger assemblies additionally benefit from an elastic averaging effect that lowers the overall error of the structure as well [67].

Most of the prior discrete architected lattice systems have been manually assembled, limiting their overall applicability. However, the robotic systems in [13,58] are designed to assemble load bearing architected lattices out of repeating unit cells, or voxels. The goal of this is a building system where the assembler size is decoupled from the ultimate structure size. Robots and voxels are designed to mechanically error-correct, so relatively simple robots may be used to achieve precise assembly [68]. In this way, many of the challenges associated with building in free space are circumvented, as the robot operates only within the well-defined space of the voxels and relies significantly on mechanical alignment features to navigate and locomote. The system presented in [13], for example, manipulates blocks at a similar size to the bricks in the commercial HadrianX [34] bricklayer system, but can navigate and build without a real feedback system, while the HadrianX system is built up around a proprietary large-scale multi-DoF stabilizer, similar to the robotic arm on a crane system in [69]. Although these prior voxel assembly systems were primarily developed for aerospace

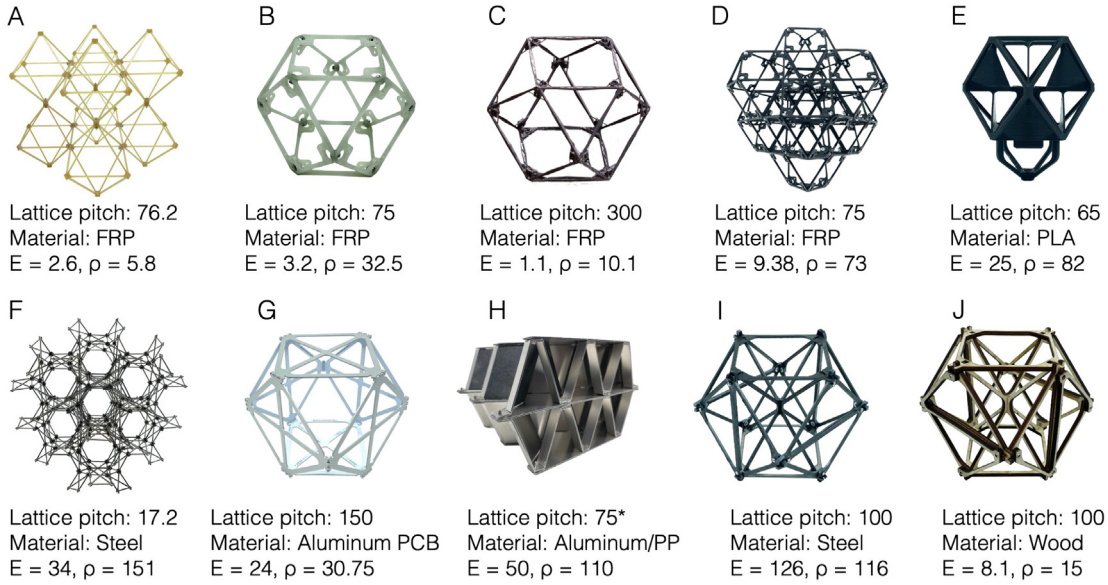

Fig. 1. Summary of the considered voxel types, indicating lattice pitch in mm, base material family, compressive modulus E in MPa, and density ρ in kg/m^3.

applications, they also have potential for building construction. [14] adapted the voxel system from [66] for use with a partially bio-based resin reinforced with recycled carbon fiber, and compared the resulting voxel's performance against some existing construction approaches, demonstrating a lower embodied carbon value. In this study, they only consider a load-bearing wall and use a manually assembled voxel feedstock. However, one of the main appeals of the voxel system is the potential ability to construct overhanging elements, such as roofs, using on-site using robots. So, there is still substantial space to more thoroughly evaluate the performance of voxels for a construction application. These prior results suggest that the assembly of voxels using relatively simple and cheap robots may represent a mass-efficient (and therefore more sustainable) approach to construction without requiring large machine or robotic systems.

3. Methods

We proceed to compare 3-D printed concrete, precast modular reinforced concrete, concrete masonry units, cold-formed steel framing, and stick framing against multiple voxel-based approaches for a simplified single-story structure. The construction consists of four walls and a roof with length 10 m, width 5 m, and height 3 m, as shown in Fig. 7. To achieve a similar level of finish in each building approach, we add external and internal sheathing to the framing and voxel based approaches. For each approach, we also add insulation for equivalent thermal performance.

Based on these parameters and finishes, we generate estimates for material consumption, fabrication time, overall cost, and embodied carbon for each of the building approaches. We evaluate the embodied carbon using the kilograms of CO_2 equivalents (CO_2e) for each approach, considering the production of the raw material, the processing of the building material, and the machine use in the construction process. The following subsections provide a summary of each building approach as well as a description of the hardware developed for this work. The embodied carbon and cost figures are provided in Table C.3 in Appendix.

3.1. Voxel approaches

In this subsection, we assess the feasibility of using voxels to construct a building. We begin by comparing the mechanical performance and sustainability of voxel designs reported in the literature. We take results from this evaluation to inform the design of a new set of voxels and a robotic assembly system. Finally, we describe the key parameters of the evaluated voxels, the details of the newly developed designs, the robotic system, and the methods used to derive the CO_2e emissions, cost, and assembly times for each approach.

3.1.1. Voxel types

We evaluated eleven types of voxels for their suitability for use in building construction; eight of these are from the literature, and three are developed for this work. With the exception of [14], much of the prior voxel research has focused on applications outside of construction, so the systems are not necessarily optimized for the requirements of building construction. Additionally, robotic assembly has not been demonstrated for the majority of the evaluated voxel types, except the voxels developed for this work and the voxels from [13].

The evaluated voxels span several lattice types and multiple material and manufacturing families. These are summarized in Fig. 1, which additionally notes the lattice pitch in millimeters of each voxel (that is, the side length of the bounding box around a single unit cell of the lattice), its general material family, and its compressive modulus and density. We provide a summary of the lattice geometries, materials, and manufacturing methods in this section, while a detailed description of how the material costs and CO_2e emissions were found is available in Appendix A and summarized in Table 1.

Fig. 1A shows a 2 × 2 × 2 block of node-connected octets from [60] made from polyetherimide (PEI, brand name Ultem 2200) plastic with 20% glass fiber reinforcement. [60] additionally developed a 50% carbon fiber version (RTP based) in the same geometry, which is not pictured, but is considered in this work. Both are made via injection molding of the entire octet cell. We refer to these as the "GFRP node connected octet" and "CFRP node connected octet" hereafter.

Fig. 1 B, C, and D are all face-connected cuboctahedra ("cuboct"). Fig. 1B is made of 30% glass reinforced nylon 66 (Zytel 70G33L). We refer to this voxel as the GFRP cuboct. 1C is made from 50% carbon fiber reinforced nylon (Stat-tech NN), which we refer to as the CFRP cuboct. Fig. 1D ("bio-cuboct") was developed in [14] as a more sustainable version of the GFRP cuboct from [66], and is made from a partially bio-based PTT with recycled carbon fiber reinforcement.

We evaluate three metals-based approaches from the literature. Fig. 1F depicts a reinforced Kelvin lattice made from laser-cut mild steel from [62]. We include this lattice as an example lattice made from

Table 1
Summary of carbon intensity, specific modulus, unit cost, and cost relative to compressive modulus of all voxel types.

Voxel type	Carbon intensity $kgCO_2e/kg$	Specific modulus $MPa/\frac{kg}{m^3}$	Unit cost USD/ kg	Unit cost per modulus USD/ kg/ MPa
Aluminum Cuboct (G)	30	0.78	14	0.58
GFRP Node-octet (A)	12	0.45	40	15.38
CFRP Node-octet (A)	19	1.37	172	21.58
GFRP Cuboct (B)	5	0.10	385	120.31
CFRP Cuboct (C)	13	0.11	79	71.82
Steel Kelvin (F)	4	0.23	13	0.38
Bio-Cuboct (D)	5	0.13	210	22.39
Expanded Miura (H)	9	0.45	28	0.56
PLA Octet (E)	3	0.30	22	0.88
Steel Octet (I)	2	1.09	7	0.06
Plywood Octet (J)	1	0.54	8	0.99

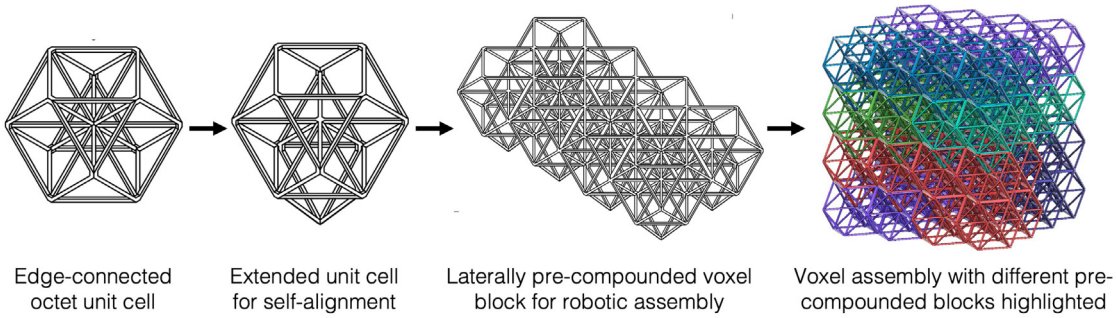

Fig. 2. Modified edge-connected octet lattice for voxel design.

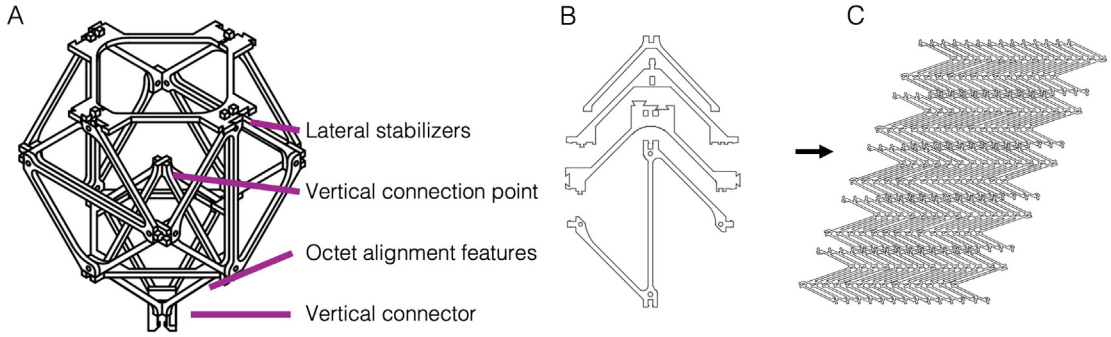

Fig. 3. Efficiently packable 2D decomposition of the extended edge octet unit cell.

purely 2D components which does not consider efficient material usage in its production. Fig. 1G is of a reinforced aluminum cuboct lattice with integrated electronics from [64]. We include this as an example of a structural voxel system with integrated electronics, to help evaluate the feasibility of this approach for applications that may benefit from electronics functionality. Fig. 1H shows a discretely assembled plate lattice from [70]. Unlike all of the other evaluated voxel approaches, this approach is based on plate lattices, as opposed to truss lattices. The lattice is formed using an expanded Miura pattern and made from folded aluminum-polypropylene sandwich material (Hylite, 0.2 mm thick aluminum on either side of a 0.8 mm thick PP core) cut on a large-format CNC cutter.

For this work, we developed a new voxel geometry aimed towards easier robotic fabrication that we produced using FFF-printed PLA, laser-cut mild steel, and laser-cut plywood. The PLA version aims to facilitate prototyping, while the steel and plywood versions are aimed at providing suitable mechanical performance using more traditional construction materials. The PLA version is shown in Fig. 1E, while the steel and wood versions are in 1I and 1J, respectively. These form an edge-connected octet lattice, and are discussed in more depth in the following section.

3.1.2. Voxel designs for robotic assembly

We developed the three voxels shown in Fig. 1 E, I, and J for compatibility with robotic assembly. The PLA octet is largely intended as a prototyping tool for convenient use to test the robots with, while the steel and plywood versions are intended as efficiently packed 2D decompositions of the lattice more appropriate for potential future use in large structures.

This new design, intended for robotic assembly, exploits the geometry of semi-regular spatial tilings to form structurally-active self-alignment features. Each face-connected cuboctahedral cell can also be interpreted as face-centered cubic (FCC) octahedral voids. Fig. 2 shows our approach using this property as a self-alignment mechanism: by shifting the FCC octahedral void downward by half its height, we generate self-aligning legs for the building blocks. From there, the unit cell is pre-compounded into larger blocks (such as the 2x4x1 block shown, or staggered block elements) that can then assemble

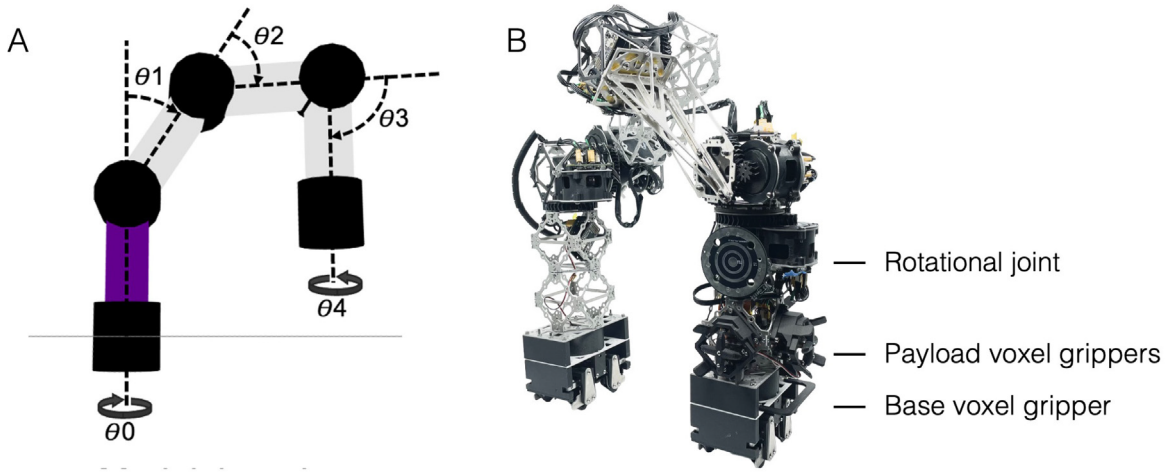

Fig. 4. Inverse kinematics model and physical hardware of the modular inchworm lattice assembler robot (or MILAbot).

into larger structures, such as the 4x4x4 cube shown, with different pre-compounded elements highlighted in different colors. To facilitate faster robotic assembly, these extended fabrication unit cells are pre-compounded into larger blocks, such as the 2x4x2 block shown in Fig. 2, or into staggered blocks, so that they can tile into arbitrary 3D shapes, forming a fully connected structure.

The interlocking voxel geometry constrains every degree of freedom except for the installation direction. There are many possible options for constraining the final degree of freedom, in this case the vertical connections, but for this design we use a snap fit connection at the base of the extended octet, as shown in Fig. 3. Lateral stability is provided by a combination of the nested octet as well as extended dovetail features along the upper plane of the voxel. This joint system is designed to enable a load-bearing connection without needing the robot to access the connection plane or location, which improves assembly speed. However, it is possible to use a variety of other options. For example, [13] uses a custom symmetric rotational connector that is actuated by a robot internal to the lattice, while [60] uses standard screws, [66] uses rivets, and [62] uses a shear clip. These joints are designed such that their overall impact on the behavior of a lattice assembly is minimized, and this nesting octet lattice decomposition enables loads to be effectively transmitted through the structure despite partial connections between lattice blocks, which can seen in the bending behavior of some of these assemblies, as shown in Appendix B.

The nesting octet–cuboct structure creates cascading envelopes of mechanical error correction that force newly placed voxel blocks into the correct position, with the overall error governed by the manufacturing tolerances of the original lattice production method. In the horizontal plane, the design permits errors up to $\frac{p}{2} - 2 \quad t$, where p is the lattice pitch, and t is the beam thickness, assuming constant thickness beams throughout the voxel. For the PLA voxel, this value is ±25.5 mm, for the steel voxel it is ±44 mm, and for the wood voxel it is ±42 mm. Because the voxels can be compounded into blocks of different shapes, the exact amount of permissible horizontal-plane angular error varies, but for these three designs, errors within ±9 degrees from the longitudinal pivot of the endpoint of this line are allowed. These provide large boundaries within which voxel blocks can be successfully and repeatably attached. Additionally, the simultaneous placement of multiple unit cells at once, and as the structure gets larger, these voxel systems will benefit from an elastic averaging effect that can overall reduce the error associated with a given build [63].

To facilitate easier fabrication, the designs of the plastic, steel, and plywood octets diverge from the basic octet geometry. In the case of the PLA voxel, because it is FFF 3D printed, flanges are added to the overhanging features to enable support-free printing. For the steel and wood voxels, the faces are split into halves to enable better packing on sheet stock, as shown in Fig. 3. With this 2D decomposition, we are able to achieve a peak continuum packing density of just under 45%. As this still represents significant material waste, a potentially interesting avenue for future work would be to consider optimization methods for adjusting the voxel decomposition to facilitate improved nesting density towards lower embodied carbon values.

3.1.3. Robotic assembly system

To make more accurate projections about the assembly speed, cost, and energy consumption of a voxel-based construction approach, we developed a new mobile robotic assembler system. Our robot is based on the inchworm-style paradigm used in [58,68], and [13]. Our system, called the Modular Inchworm Lattice Assembler robot, or MILAbot, is a five-degree-of-freedom robot that traverses a voxel structure using grippers on both ends, and can deliver and place a voxel payload using three additional voxel grippers. The MILAbot is shown in Fig. 4 for reference.

The MILAbot operates by carrying larger compounded blocks of voxels and adding them to the structure by dropping the blocks and engaging the snap-fit connection. Larger structures are built up by staggering the blocks such that the entire structure is fully connected, while the protruding octet, snap-connection, and dovetails provide stability under bending and tensile loads, as discussed in the prior section. By building with pre-offset blocks, the MILAbot is able to assemble first layers and overhangs. The intended workflow of this system is that voxels are pre-compounded into larger blocks via an automated system and then delivered to site where they are then assembled into larger structures by the MILAbots. The development of an automated system for this pre-compounding is beyond the scope of this work, but because this would occur in a controlled environment for relatively small structures, we anticipate that it would be possible to leverage existing high DoF gantry or robotic arm systems, which have been used to produce structures of similar or higher complexity [71–73] in a similar manner to pre-production proposed in [10] or [46].

The MILAbot is controlled through a Web-based real-time digital twin simulation tool, as shown in Fig. 5A. Structures may be either imported as mesh geometries and then voxelized, or may be designed by hand with a point and click interface. From there, robots and voxel feeds are placed, and the structure is partitioned between the robots, and an assembly sequence is determined. Partitioning is based on grouping the voxels based on distance to a voxel feed, such that there is no overlap between different robot domains, which innately prevents collisions. Once an assembly sequence is determined, robot

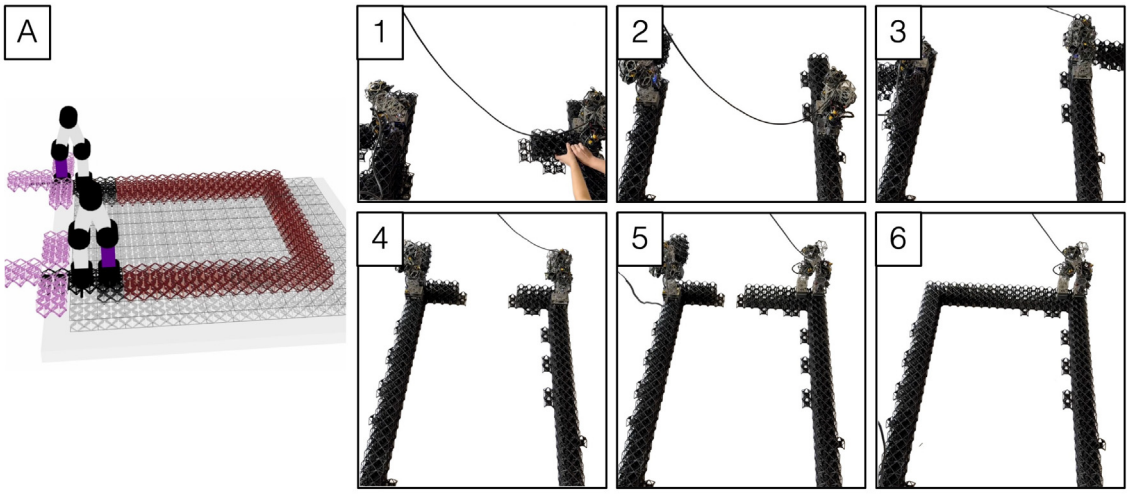

Fig. 5. Overview of the robotic assembly of a doorframe, showing the digital twin control space and key frames of the assembly sequence.

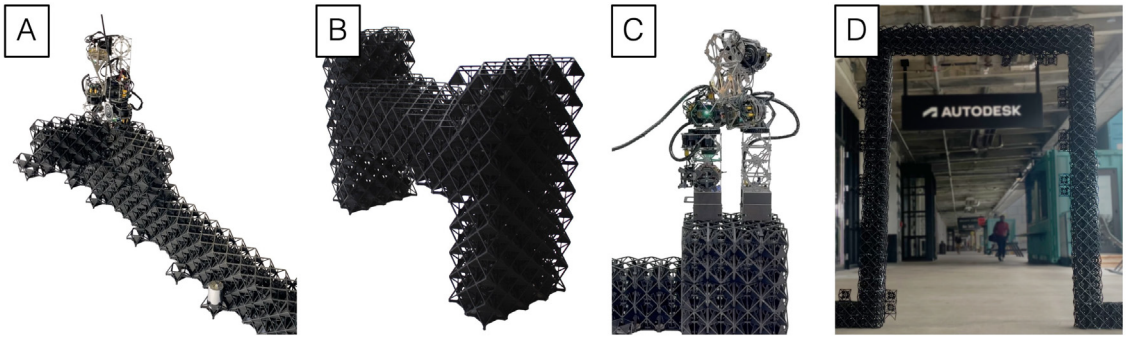

Fig. 6. Example robotically-assembled meter-scale voxel builds.

paths are determined based on a modified A* algorithm as described in [68] as this provides good performance even over large structures. At each step, commands are streamed from the digital twin to the physical robots over Wi-Fi. A more complete technical description of the implementation and validation of this system is available in [74].

An example assembly sequence is shown in Fig. 5. First, voxel blocks are manually fed to each robot. Then, the robots step forward and iteratively place new voxel blocks, returning to the feed to pick up new blocks. In this sequence, the robots assemble a doorframe flat on the ground, which we then tilt up, as shown in Fig. 6. Note that the fringes that are visible on the built doorframe are the result of using compounded voxel blocks with extra voxels added on the sides to act as lateral stabilizers, as this assembly demo was done on top of a cloth backdrop that we could not rigidly fix the voxel feeds or any of the first layer voxels to. In a "real" first layer build, this would not be necessary, as we would anticipate that the first layer of voxels would be anchored a foundation.

We used the MILAbots to assemble a set of meter scale objects to determine the assembly throughput of the system, as well as to better understand its limitations. The assembly demos are shown in Fig. 6. Based on these, we determined the average time per movement of the robot as 9.5 s and the average power consumption as 13.3 W. We additionally identified some key limitations of the hardware.

The first significant limitation is that the robot is unable to climb vertically, which means that it needs to build a support staircase or to assemble horizontally and then tilt up, as in the case of the doorframe. This limits its ability to scale to larger structures, as the footprint and assembly time for the stairs also grow increasingly large. So, we proposed that a more scalable system might use a vertically actuated voxel feed, which engages with the voxel structure equivalent to a pinion gear on a rack, similar to what is proposed in [75]. Although this is not yet implemented in hardware, we implemented it for the simulation software to extrapolate assembly time estimates.

Next, our system currently uses manually fed voxels, which is also a significant limitation on the throughput of the system. This will also need to be automated if the system were applied to the architectural scale. The goal would be to have a flat-packed stock of parts that would be assembled on site by a desktop-scale CNC, with the assembled voxels then distributed to the MILAbots via an automated system.

Lastly, the actuators in the robot use 3-D printed gearboxes that fatigued and eventually failed during our testing. For the purposes of making a more accurate cost estimate, we replace all of these components with an equivalent metal off-the-shelf reduction. This takes the total cost of a single robot from $750 to $1250. To account for the cost of an elevator system, we then increase the estimated per-robot cost to $1875.

3.1.4. Structural elementdesign

After determining the relevant parameters of the voxels and robotic assembly system, we designed the overall voxel building. The simplified building consists of a fully enclosed 5 × 10 × 3 m box with approx. 610 mm spacing between framing elements. The structure is sheathed internally and externally with 1/2" oriented strand board (OSB) and a 100 mm thick layer of expanded styrene foam (EPS) insulation. The wall studs have a square cross-section formed by voxels, while the roof joists have an I-beam cross-section formed by voxels. This is shown in Fig. 7.

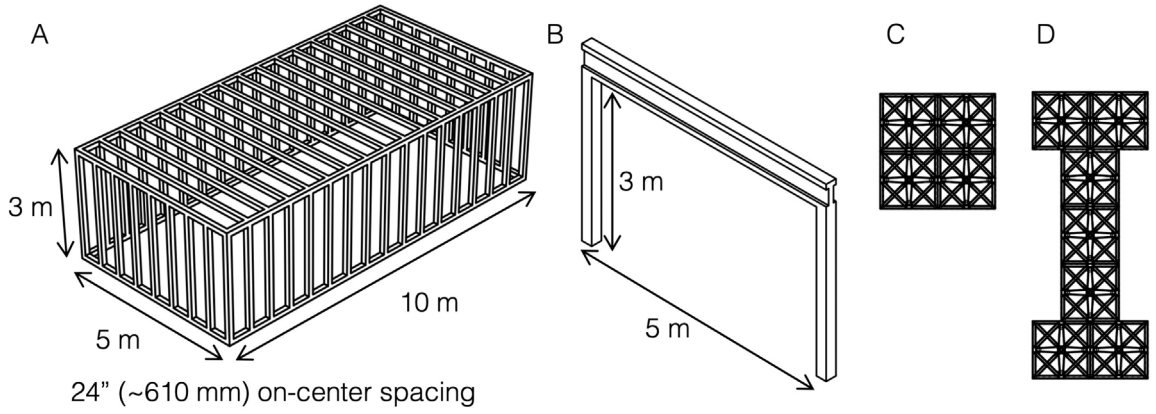

Fig. 7. Diagram of the simplified structure used for our estimates, showing the base plan for the 24" (610 mm) on-center spaced stud framed 5 m × 10 m × 3 m building, the single spanning frame element used for evaluating the voxel approaches, and example cross sections of the stud and joist elements.

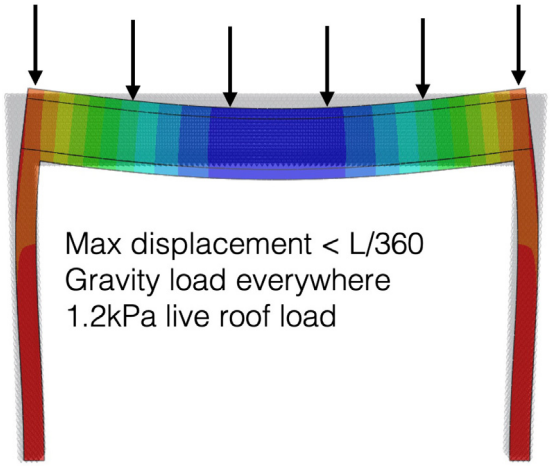

Fig. 8. Overview of the evaluated loading scenario, with a 30x deformed model overlaid on top of the undeformed structure.

We determine the required quantity of voxels for the structure by treating each 5 m-long 3 m-tall spanning element (consisting of a stud on either side with a joist over the top) as an individual structural element that needs to support its own self weight, that of the sheathing and insulation on it, and an additional 20 p.s.f live roof load based on the requirements in the ASCE 7 [76]. We then increase the dimensions of the framing element until the maximum displacement is below the L/360 standard [77]. This is summarized in Fig. 8.

To evaluate the structural performance of each archway (the stud-joist-stud spanning element shown in Fig. 8), we performed Finite Element Analysis (FEA) to determine the maximum deflection under a consistent load case. To achieve this, we developed a simulation framework using Python-Abaqus scripting. The script generates the arch geometry based on the specified stud and joist cross-sectional properties. We treat the mechanical properties of the voxels as the properties of the bulk material in each archway. Depending on the voxel type and the availability of the data, the Young's modulus is typically derived from compressive modulus measurements of either single unit cells or assemblies up to 4 × 4 × 4 voxels. Density values all account for the mass of connectors in addition to the voxels themselves. The script then defines the boundary conditions: the bases of the beams are fixed, a gravity load is applied, and a pressure load is imposed on the top surface. Due to the geometric variability of the models, the pressure load is calculated such that the resulting equivalent point load is 3.66 kN. The generated solid is then meshed using C3D10 tetrahedral elements. We chose this element because it is easy to automate while offering 10 nodes, quadratic interpolation, and four Gaussian integration points, ensuring good accuracy and a proper representation of the field variations across the element. The mesh size is half of the voxel height value. Finally, the script runs non-linear analysis and, once converged, records the maximum deflection of the horizontal beam in the vertical direction. This code is provided in Appendix B.

While treating the voxel mechanical properties as equivalent to that of a bulk material is a simplification, prior work indicates that the voxel behaviors extrapolate well: one of the key objectives behind each voxel design is for the geometry of the lattice to dominate over that of the joints and behave as a bulk material with equivalent properties. Prior work has established that joint effects are second order compared to that of the beams [66]. In line with this, discrete systems achieve similar performance to their continuously manufactured counterparts. For example, the discrete lattices in [12] exceed the performance of the continuous microlattice described in [61], while the voxel system in [60] achieves comparable performance to the continuously manufactured lattices in [59], indicating that behavior of the beams dominates.

To better validate our modeling, we set up four samples of voxel beams to test under 3 point bending as a physical and virtual experiment. These results indicate strong alignment between the physical discrete assemblies and their virtually modeled continuum material counterparts. The full results and description of this are available in Appendix B. However, it is important to note that our results here are based on a first order approximation of the actual system, and that real deployment of any of these systems would require more physical testing as well as more system-specific validation of FEA tools and workflows.

In larger assemblies, manufacturing tolerances and cumulative geometric slack can introduce localized nonlinearities that deviate from idealized bulk behavior. The voxel systems considered here are designed with geometrically constraining node interfaces to minimize slip accumulation and error propagation across scales. Although prior experimental studies have shown that stiffness remains beam-dominated rather than joint-dominated in relatively large assemblies [12,65], tolerance accumulation may become more pronounced in structures at the building-scale. While the modeling framework we use reflects the intended mechanical regime of these systems, it should be noted that it is an idealized approximation of the system.

A summary of all of the voxel beams, along with their maximum deflections, are shown in Fig. 9. We adjusted the cross-sectional voxel quantities until the deflections were within 2 mm of each other, and all below the maximum of 13.89 mm. As Fig. 10 shows, the dimensions, voxel quantities, and framing weights vary significantly across the different voxel approaches. This is because the voxels span a range of mechanical properties, so for an equivalent absolute load on the

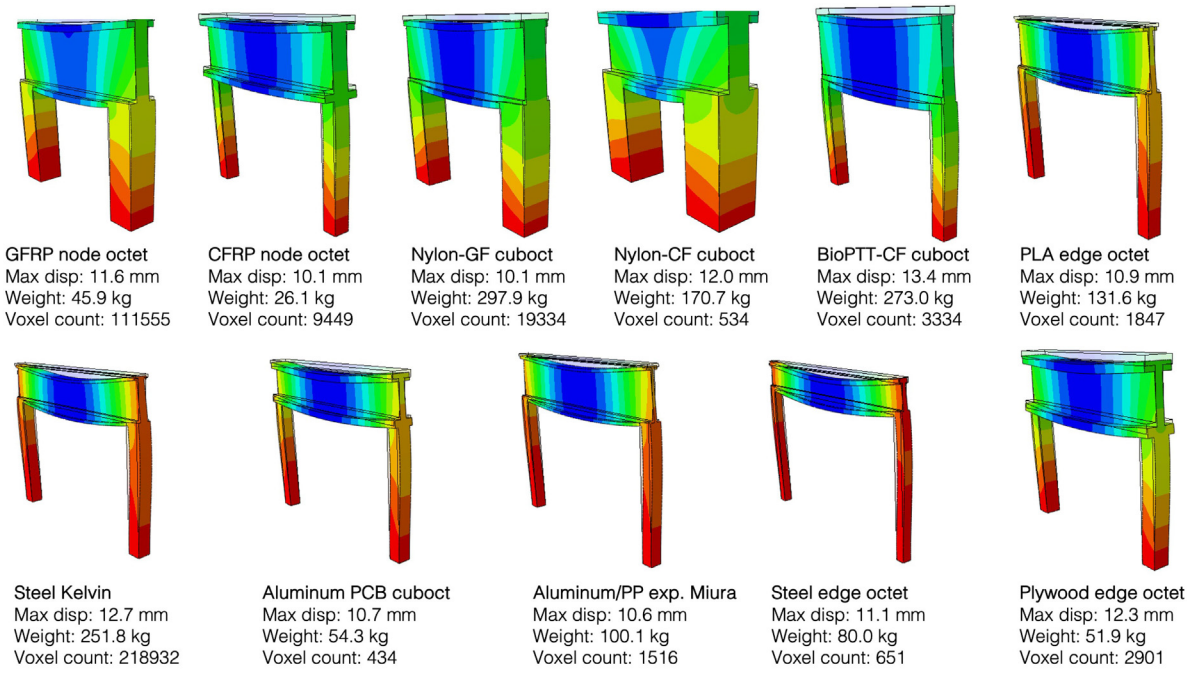

Fig. 9. All of the evaluated voxel frames, with the maximum displacement, single frame weight, and single frame voxel count noted.

roof, some voxel approaches require substantial dimensions before they reach the requisite stiffness to support it. The total weight of the framing structure is then the weight of all of the load-bearing component frames, along with the short-side stud elements (square cross-section), as well as the upper and lower shear bracing (I-beam cross-section), as shown in Fig. 7A.

We projected the assembly speed for each of the frames by determining the average number of actions per placed voxel for a single structural framing element using an elevator-style voxel feed. "Actions" are defined here as each robot step type and each voxel placement type, which are structured as two-move sequences to return the robot to the same starting configuration, with the legs placed two voxels in x or y away from each other. For example, the single action of "step forward" consists of moving the relative front leg forward to a spacing of four voxels horizontally away, and then moving the back leg to close the gap. Voxel placement movements are similarly structured, so a placement movement looks like swinging the back leg into the placement position, placing the voxel, and retracting back to the default position. Essentially, the library of actions consists of all steps that can move the robot two-voxel distances laterally, up to two-voxel distances laterally and vertically, or place a new voxel block within that bounding envelope. Because of the relatively similar distances traversed during each of these movements, and because of the reliance on mechanical alignment features over precise robot control, all of these steps take roughly a similar amount of time, allowing us to extrapolate approximate robot throughput speeds based on the amount of actions taken during a build.

Using this sample framing element build, this results in an average of 6.5 actions per placed voxel. At 9.5 s per movement, carrying the maximum volumetric payload of three 4 × 2 × 2 65 mm lattice pitch voxel blocks, this results in a volumetric throughput of 0.26 m^3 per hour. For our projections, we use 25% of this value to build in sufficient buffer to account for set-up and de-installation time, as well as a future voxel feed system.

3.2. Compared construction approaches

Here, we compare voxel-based approaches with 3D concrete printing (the predominant onsite automated method), precast modular concrete (a prefabricated method), concrete masonry units, cold-formed steel framing, and stick framing (manual methods). Material amounts and embodied carbon estimates are drawn from a range of sources in the literature, while overall material, labor, and equipment costs are estimated using RSMeans [78] for United States national averages.

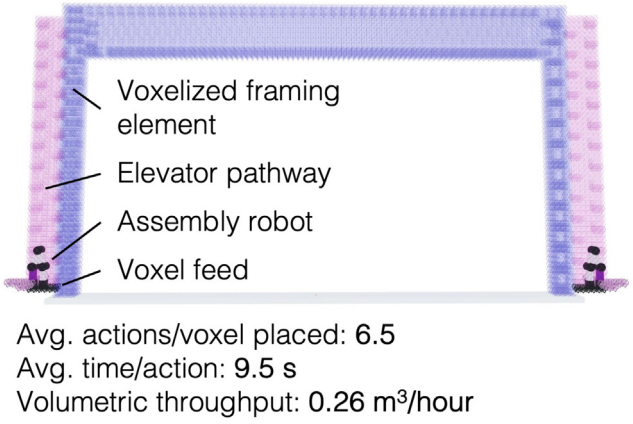

Fig. 10. One of the structural elements loaded into the MILAbot simulation space, configured for a moving voxel feed.

3.2.1. 3-D concrete printing

For the 3DCP approach, we use a 40 mm track width and a wall cross-section similar to the ones in [4,19], and [79]. The dimensions are shown in Fig. 11. Based on commercial practices, such as what is discussed in [21], we additionally reinforce the wall by casting concrete with reinforcement into the walls according to the ratios given by [79], and adding spray foam insulation to an equivalent thermal insulation rating as the EPS foam used in the voxel and other framing approaches. For the roof, we use hollow-core panels, as in [19]. The dimensions of these are shown in Fig. 11, and further discussed in the following subsection. We use the parameters of the COBOD BOD2 gantry girder printer to determine the build time. We determine the embodied CO_2e by using the values determined by [79] adjusted for our geometry.

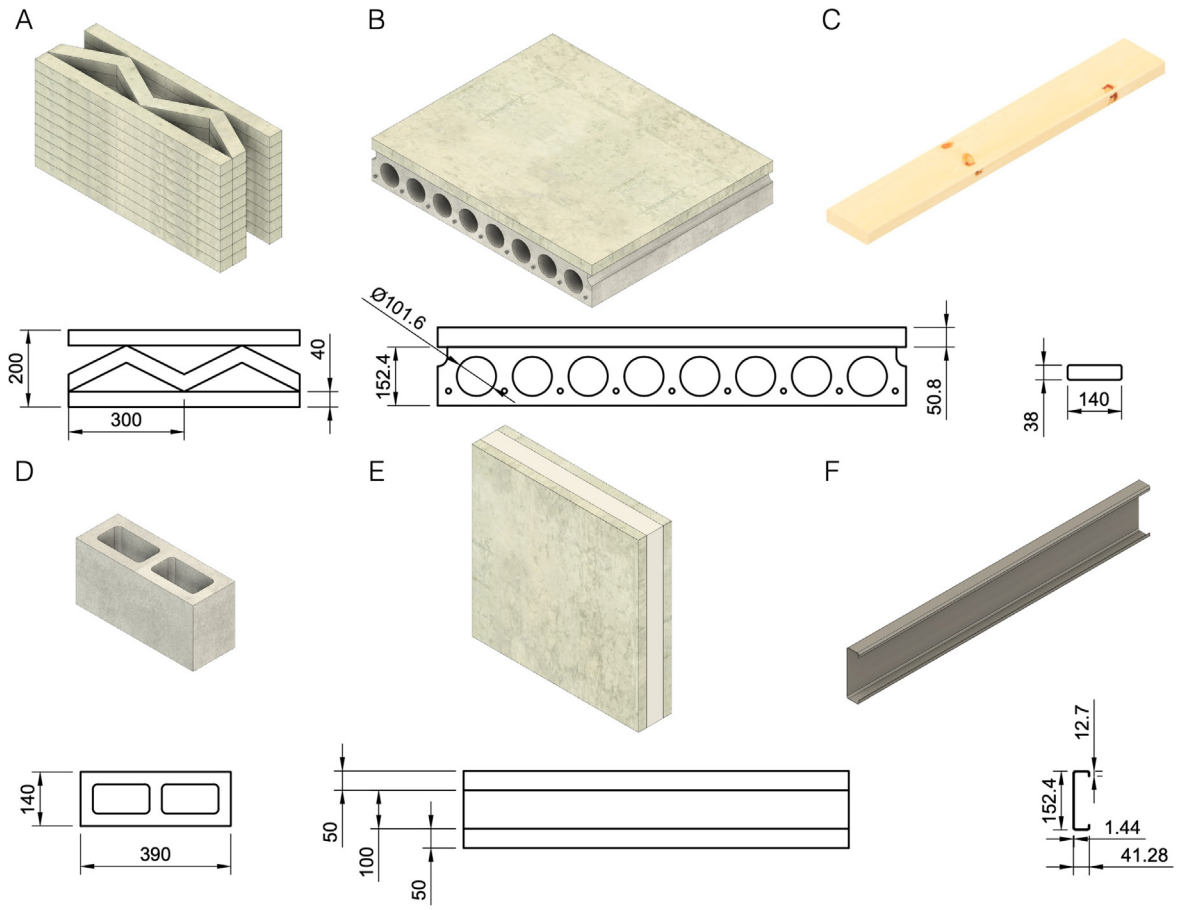

Fig. 11. Summary of key parameters of the existing construction techniques that we compared against. All dimensions in mm.

From this, we get an embodied carbon value of 17338 kg CO_2e, at a total weight of 46,267 kg. Using the BOD2 maximum printing parameters [80], the total time to print the walls is only 10.4 h. Based on the BOD2 recommendations, we estimate another 10 h for total set-up and de-installation time, with four printer techs on site at $30/h for the entire print use time. The addition of concrete reinforcement, insulation, and pre-cast roof panels then adds another approximate 100 h of build time, for a total assembly time of 119.7 h. The overall material cost for the entire structure is $12,972.95, while the combined labor and equipment cost is $7616.13. To estimate the cost of using the printer, we assume a five-year 5000-h/year use schedule of the printer that we amortize its base cost ($600,000) over, in addition to the cost of the electricity needed to run it, using the 2023 Massachusetts average rate of $0.34 per kilowatt hour, similar to the method used in [4]. This results in a total cost $20,589.08 for the 3DCP building.

3.2.2. Precast modular concrete

For the precast modular concrete approach, we use insulated sandwich panels for the walls, [81], and hollow core panels for the roof, as done in the 3DCP case. These are chosen according to [41] to meet the loading requirements and spans of the sample building. The insulated sandwich panel, as shown in Fig. 11 consists of two 50 mm thick reinforced concrete slabs around a 100 mm thick EPS foam insulating layer. The concrete slabs are reinforced at a ratio of 33.5 kg/m^3, lower than the reinforcement ratios provided by [19], and more in line with guidelines given by [41]. The roof panels are then made of a 6" (152 mm) tall hollow core panel with a 2" mesh reinforced concrete topping. The cross-sectional area of the hollow core panel alone per 4-foot (1.2 m) section is 0.12 m^2 and has 9 strands of 9.42 mm diameter steel reinforcement. The topping is reinforced at 0.25% of its cross-sectional area. We assume all the concrete in the structure is the same blend, given by what is used in [79] . The total weight of this structure is then 42114 kg, with an embodied carbon of 11899 kgCO_2e. The total material cost is $23,681.24, while the fabrication cost is $2676.99, for a total cost of $26,358.23. The assembly time is 54.25 h. For this approach, and the remaining manual approaches, the cost and time estimates are generated using only RSMeans data, as previously discussed.

3.2.3. Concrete masonry units

The concrete masonry unit wall is designed according to reinforcement ratios given by [79] and adjusted for our dimensions. Like [14], we use 140 × 390 × 190 mm CMUs. We use the same hollow core panels for the roof as in the prior two concrete building examples. We also add a single layer of EPS foam insulation and OSB sheathing internally to the structure. The total weight of the structure is 48022 kg, and the embodied carbon is 14005 kg CO_2e. The material cost is $14,250.24, and the labor and equipment cost is $9822.80 for a total cost of $24,073.04. The total build time is 209.03 h.

3.2.4. Cold-formed steel framing

The cold-formed steel framing follows the same basic pattern as the voxel framing scenarios, though we use a constant cross-section throughout the structure. The dimensions of this are shown in Fig. 11 and are taken from a product listing for a 16-gauge 6" stud [82]. For the roof joists, we place these back-to-back for added stability and verify that the structure deformation is below the L/360 standard under the same loading conditions as used for the voxel approaches. Sheathing is then added as in the voxel approaches, for a total structure weight of 2074 kg. The embodied carbon is 6608 kgCO_2e. The material and labor

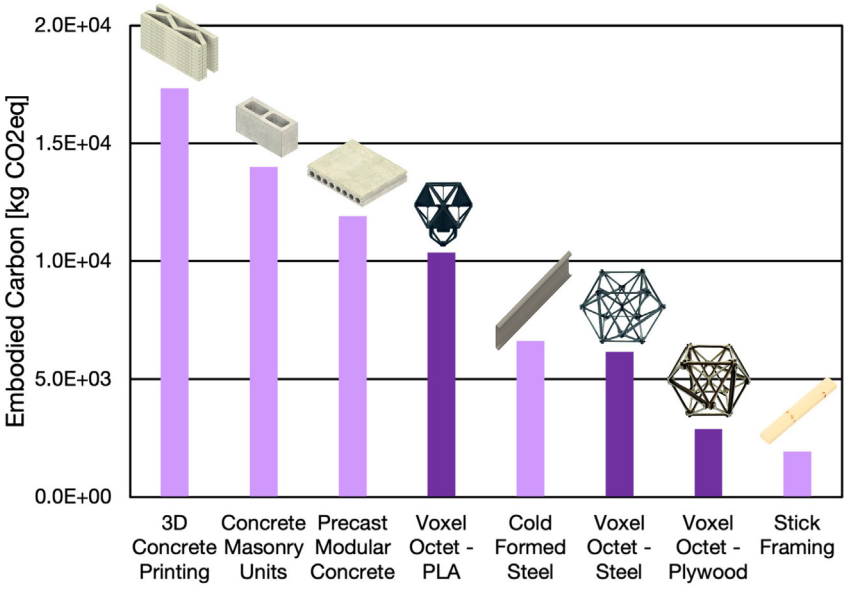

Fig. 12. Total embodied carbon for the three voxel approaches developed for this work, compared to the standard construction approaches for the complete simplified 1-story building.

costs are $15,859.03 and $10,998.60, respectively, for a total cost of $26,857.63. The build time is 282.1 h, for two carpenters working on each task sequentially.

3.2.5. Stick framing

As with the other framing-based approaches, the stick framing case follows the same stud pattern. We use 2" × 6" (real dimensions 38 mm × 140 mm) dimensional lumber as the base unit for the studs, and 2" × 12" (38 mm × 280 mm) beams for the roof joists. We use steel ties to secure the roof joists to the studs. Including sheathing and insulation, the overall weight is 1149.85 kg and the embodied carbon is 1933 kgCO_2e. The material cost is $4983.09, the labor cost is $4981.26, and the total cost is $9964.35. The build time is 108.5 h, for two carpenters working on each task sequentially.

3.3. Comparison methodology

All of the approaches are compared using results for the entire simplified building, unless otherwise noted. This means that all the calculations include the additional finishes (sheathing and insulation), so that the comparisons are at an equivalent level of finish. For example, for the voxel approaches, this means that the time calculation is based on the robots first assembling the framing structure, and later a team of two carpenters insulating and sheathing the building sequentially. Similarly, cost accounts for price of the voxels, as produced by a vendor, amortized material cost and electricity costs of the robots, labor costs to supervise the robot build, and the material and labor costs for the traditional construction activities. For cost data from RSmeans, the base cost is taken to be comparable to how voxel costs were determined.

The embodied carbon assessment follows the principles of ISO 14040/14044 [83,84], and is intended as a comparative assessment of alternative structural systems, as opposed to a complete cradle-to-grave LCA. The system boundary is limited to cradle-to-gate material production, corresponding to A1–A3 in EN 15804, encompassing raw material extraction, processing, and manufacturing. Construction stage activities, use phase impacts, and end-of-life scenarios are excluded, with the exception of the automated methods (3DCP and voxel approaches), where we factor in the electricity cost of running the automated systems in the overall calculation, as we consider this a necessary part of producing the material. For biogenic materials, we use the figures from [85], which covers A1–A3 modules, and excludes any biogenic carbon flows. Material quantities are derived from the previously described structural designs, including all additional sheathing, insulation, and fastening beyond the structural elements. For the voxel based approaches that leverage subtractive methods, i.e. the plywood and steel voxels developed for this work, the aluminum PCB voxels from [64], the steel Kelvin voxels from [62], and the expanded Miura plate lattice from [70], we include the off-cuts in our overall material consumption, as this represents a potentially non-trivial amount of material waste in the process. Under these assumptions, the embodied carbon results presented here are intended to support relative comparison of structural strategies and construction paradigms, rather than to provide absolute environmental impact values for specific buildings.

4. Results and discussion

In this section, we compare and evaluate the voxel approaches against the existing construction approaches in terms of their sustainability, cost, and building speed. These criteria reflect primary environmental, economic, and logistical drivers in construction decision-making. While other impact factors are relevant to the environmental sustainability of a construction approach, we use embodied CO_2e, as this metric is widely reported and allows consistent comparison across systems. A complete summary of these parameters is also available in Table C.3.

4.0.1. Sustainability assessment

We use the embodied carbon of each approach as our metric to evaluate its sustainability. While the embodied carbon of many of the voxel approaches is quite high, as summarized in Table C.3 the three voxel types developed for this work demonstrate potential sustainability benefits compared to traditional construction methods. As shown in Fig. 12, the voxel-based approaches outperform all of the concrete-based methods, while the steel and wood voxels are able to provide lower embodied carbon than every approach, aside from stick framing. Compared to 3DCP, the steel voxel approach generates only 36% the amount of the embodied carbon, while the plywood approach generates only 17% of the embodied carbon of the 3DCP approach. The emissions of the voxel approaches are more comparable with their equivalent framing-based approaches, but achieved via a potentially automated building process.

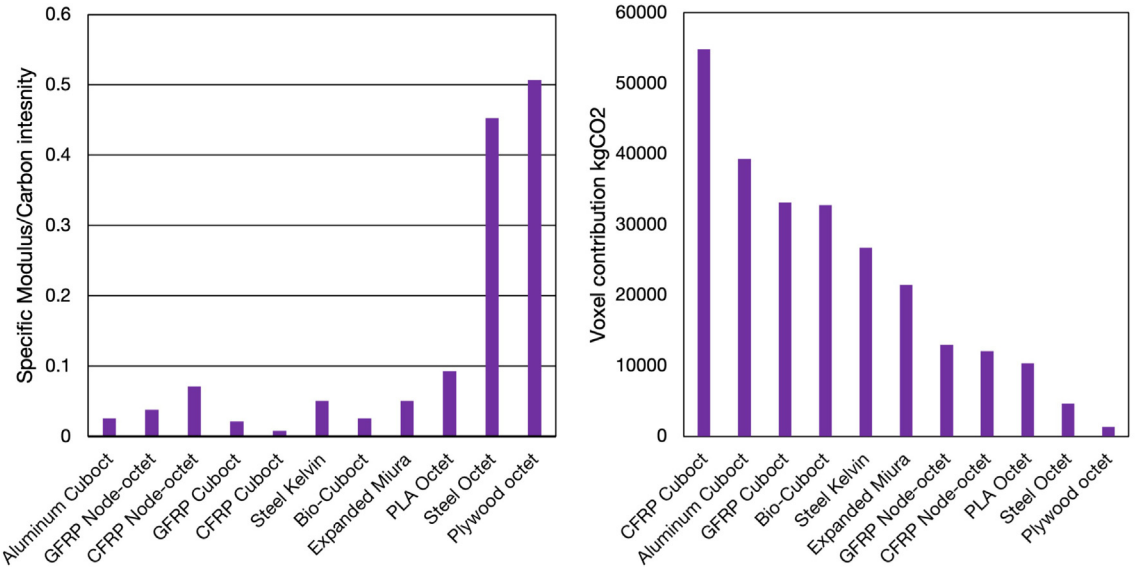

Fig. 13. Embodied carbon [kg CO_2e/kg] of the voxel approaches relative to the voxel's specific compressive modulus [MPa/ ρ] and embodied carbon of each voxel building approach, accounting only for the voxel contribution.

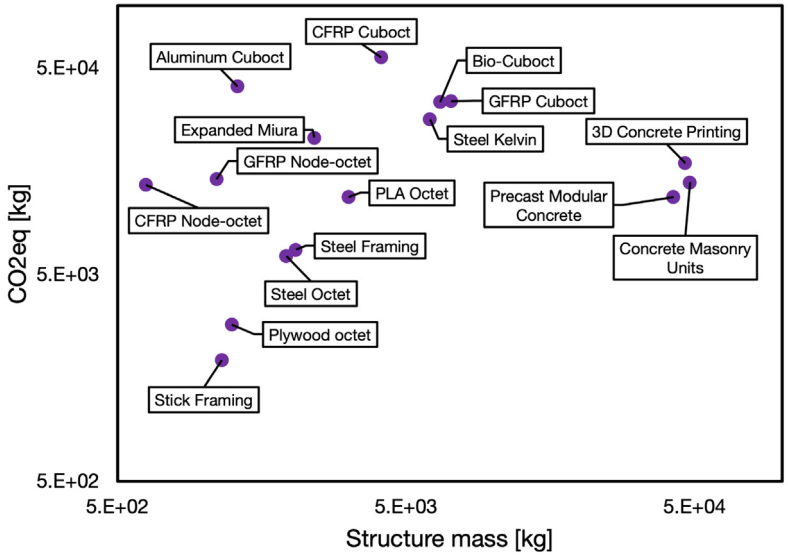

Fig. 14. Overall structure mass, including sheathing and insulation, compared to embodied CO_2e for all of the considered approaches.

However, most of the considered voxel approaches perform poorly in terms of sustainability. The voxel-only contribution to the embodied carbon is plotted for all voxel types in Fig. 13. Of the existing construction approaches, 3DCP had the highest embodied carbon value at 17,338 kgCO_2e— this value is exceeded by the voxel contribution alone for all the voxel approaches with higher embodied carbon than the GFRP node-octet.

This wide range is because while some voxels were designed for improved sustainability, most were designed only for specific mechanical performance metrics. To compare the material-sustainability efficiency of the voxels we can evaluate their specific modulus (MPa/ ρ) relative to their carbon intensity (kg CO_2e/kg). This metric helps capture the balance between the mechanical efficiency of the lattice (how stiff it is relative to its density) with its environmental efficiency (how much embodied carbon is in each unit of the material system). So, for example, although the aluminum cuboct has relatively good specific modulus at 0.78 MPa/kg/m3, this is outweighed by its very high carbon intensity of 30.17 kgCO_2e/kg.

From this metric, we see that the plywood and steel octets are significantly more efficient than the other considered approaches. This is because they are manufactured from base materials with lower embodied emissions compared to the other approaches (especially the aluminum and fiber-reinforced high-performance plastics) and produced in a way that does not waste too much of the feedstock (in contrast to the steel Kelvin lattice, which uses subtractive fabrication without considering packing efficiency). This is additionally because the chosen lattice type, the edge-connected octet, has better mechanical efficiency at the ranges needed for building loads. From this metric, the next most efficient systems are the PLA edge octet developed for this work and the CFRP node octet, which could have potential improvements through substituting their constituent materials with more sustainably efficient materials.

We can also evaluate the overall material sustainability of all the approaches by considering the ratio between their embodied CO_2e and their overall structural mass. These results are plotted in Fig. 14. As this graph shows, the concrete approaches have lower embodied carbon

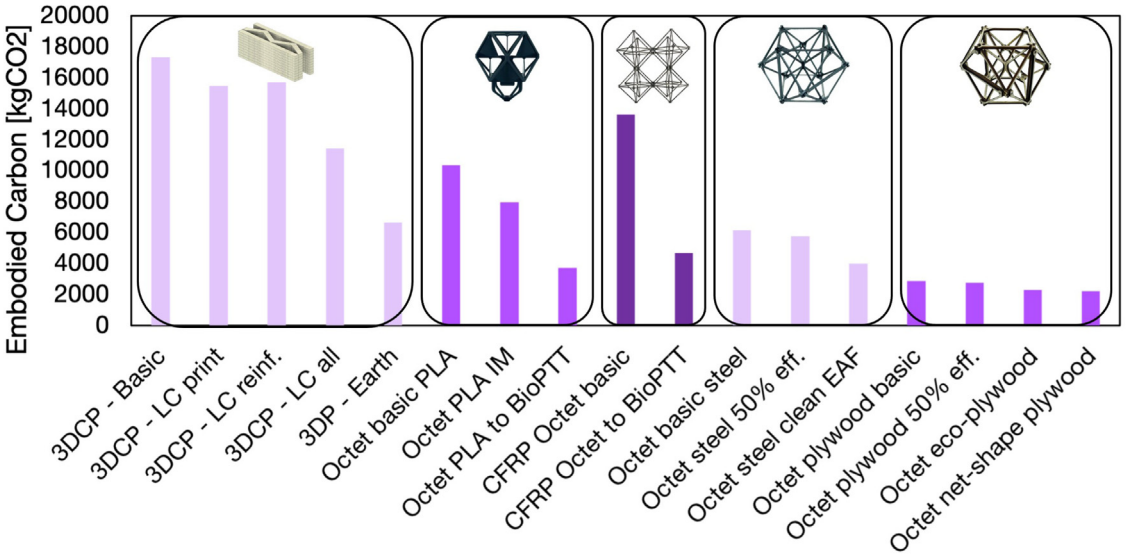

Fig. 15. Projections of the sustainability performance of 3D printing and voxel approaches with material substitutions.

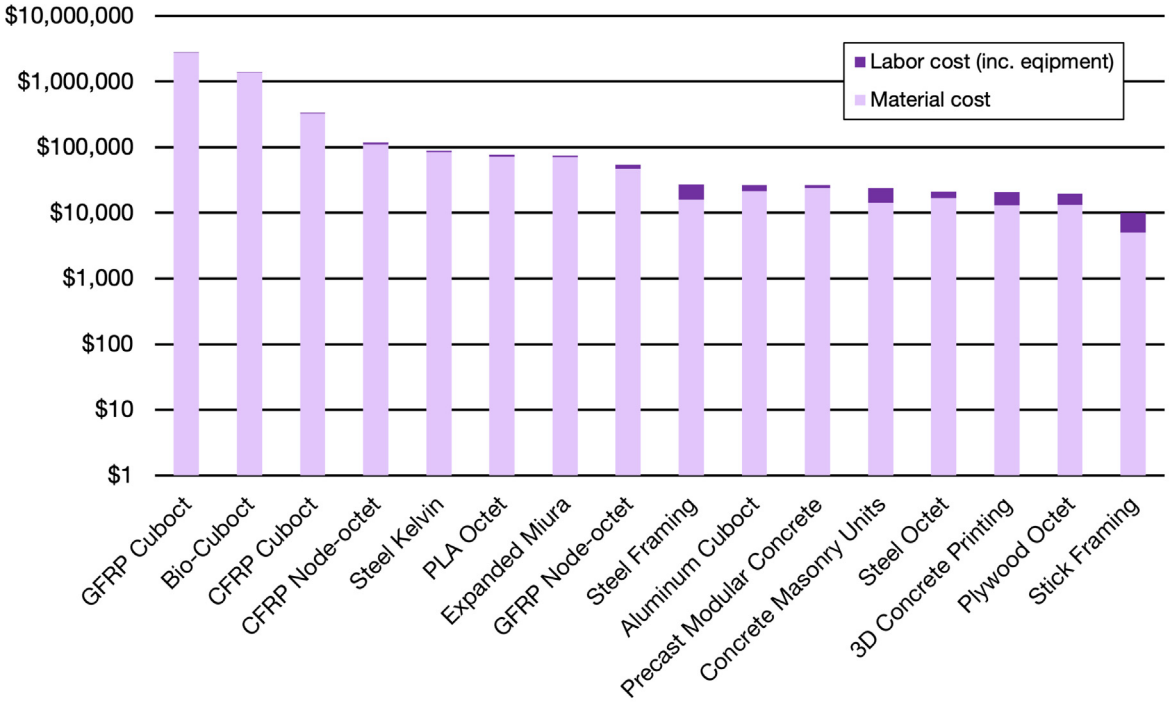

Fig. 16. Material cost, consisting of the purchased material cost of all components, and fabrication cost, consisting of the labor cost and equipment cost for each approach.

per mass than any of the other approaches. However, in absolute terms, they still have an overall high embodied carbon. This indicates that their building approaches are inefficient in terms of how mass is distributed, suggesting that work towards more efficient concrete usage could offer significant sustainability benefits. In contrast, the performance of the CFRP node-octet, for example, is already extremely lightweight, but with very high emissions, indicating that the most promising route for improving performance would be through base material substitution.

Based on these results, we additionally consider some projections for the different building approaches with more eco-friendly material substitutions. These are summarized in Fig. 15. For the 3DCP approach, we consider the impact of switching to a lower carbon concrete (denoted as LC in the graph) for the 3D printed portions, the cast-in-concrete reinforcement, and both. For these calculations, we use the figures reported in [24]. By substituting lower embodied carbon concrete for all of the concrete, we are able to reduce the embodied carbon of the 3DCP approach from 17,338 $kgCO_2e$ to 11,441 $kgCO_2e$, a 66% reduction. There is also substantial work exploring alternatives to concrete, such as printing using earthen materials, as by WASP [26]. Using the reported carbon intensities from [22], we find that substituting an earthen mixture with a low-carbon intensity, the 3D printing method can further lower to 6655 $kgCO_2e$, which is competitive with our projections for the steel octet voxel.

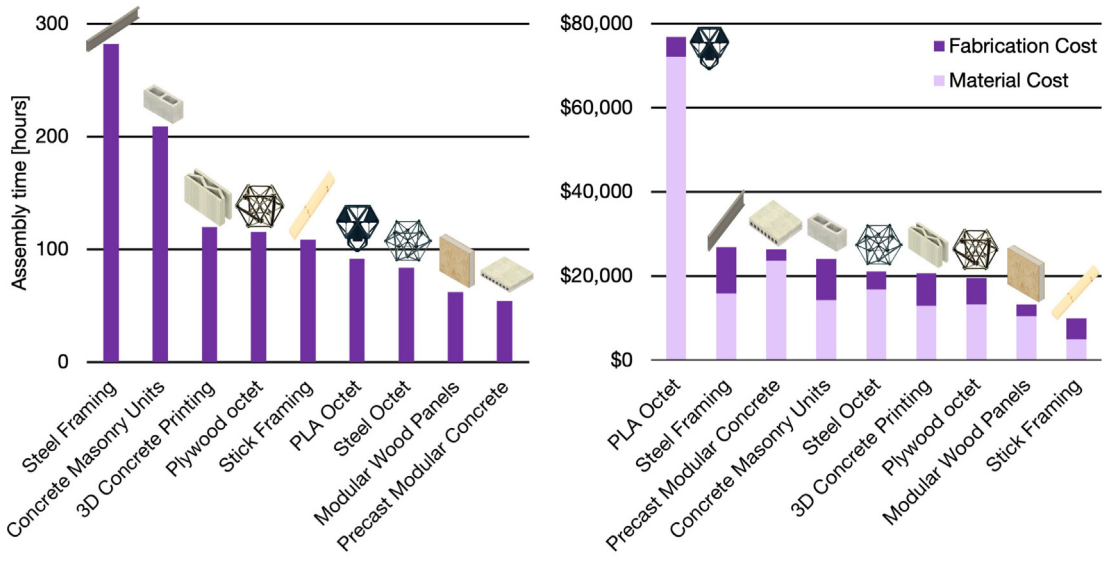

Fig. 17. Total assembly time for each approach and total construction costs of the existing construction approaches and only the voxels developed for this work.

4.0.2. Building costs and times

Cost data is determined as previously described. Note that for assembly times and labor cost calculations, for the voxel approaches, we assume a robotic swarm of 24 robots operating symmetrically over the structure, with a volumetric assembly speed that is 25% of the speed of the current hardware system, to build in a buffer for system installation/de-installation and voxel feeding. Sheathing and insulation are then manually applied sequentially after the structural assembly.

The voxel approaches span a wide range of costs; however, most of the approaches are within the same order of magnitude as the existing construction approaches. The steel and wood octet voxels slightly outperform most of the considered existing approaches. The cost of every considered approach is shown in Fig. 16. Fig. 17 shows the total assembly time for the traditional construction approaches, as well as the considered voxel approaches. Steel framing is the slowest approach, at 282 h, while precast modular concrete is the fastest at 54.3 h. The voxel approaches fall in a similar range as the stick framing and 3D concrete printing approach.

The stick framing-based approach is by far the cheapest approach in total, while the steel-framed approach is the most expensive of the existing construction approaches. The total cost of both framing approaches is approximately evenly split between labor and material costs, representing the highest proportional contribution by labor of all the considered approaches. On the other side, the pre-cast modular concrete approach has the lowest labor contribution of the considered approaches.

Given the low labor costs pre-cast modular concrete and the low material costs of stick framing, it is worth considering the performance of other wood-based modular building systems. Structural insulated panels (SIPs) consisting of two OSB layers around an EPS foam interior sandwich-style panel provide a wood-based alternate construction system we can consider in relation to the voxel approaches. Projections of the speed and cost of a SIPs version of the building, based on the same RSmeans dataset, are shown in Fig. 17, along with the other existing construction approaches and the voxel approaches developed for this work.

Compared to 3D concrete printing, the voxel assembly method achieves relatively similar speeds for the structural components. The 3DCP approach only requires 20.4 h to print the walls, in addition to installing and deinstalling the printer, according to figures from COBOD [80]. The steel voxel requires 7.1 h, the PLA voxel requires 15.2 h, and the plywood requires 39.1 h, including setup and de-installation time. A significant portion of the total build time for both automated approaches is spent on sheathing and insulation (about an additional 80 h for both approaches), highlighting that efforts aimed only at automating the construction of the base structural system may be limited in the total speed improvements that they can achieve. This is emphasized by the fastest speeds achieved by the modular wood panels (SIPs) and the precast modular concrete panels, as in both of these approaches, there are no secondary passes for insulation and sheathing.

This suggests that while the robotic assembly system could achieve further throughput improvements through using higher-performance motors, increasing the swarm assembly size, or increasing its carrying capacity, the greatest potential benefits lie in additionally automating future operations, such as sheathing and insulation. The approach for this could either be sequential, that is, the mobile robots install the sheathing as a second pass, or it could be done in parallel, by developing a closed, more brick-like voxel geometry. A future system incorporating sheathing-integrated voxels might also have insulation built in, and use electronics-integrated voxels sparsely to additionally build out the wiring of the house.

In Fig. 18, we plot the assembly cost versus the assembly time, showing a relatively linear relationship between the two. This is because our cost model assumes two workers supervising the robotic voxel assembly system, as well as manually installed sheathing and insulation, so the overall fabrication cost is dominated by labor as opposed to the cost of using the robot, which is low: less than $20 for all voxel approaches, and less than $10 for the three voxel approaches developed for this work.

The amount of robots to use for a given structure represents an interesting problem. While initially throughput can be trivially increased by increasing the number of robots, this will reach a limit either physically, based on building footprint or structure shape, or based on the challenges of computationally planning for very large swarms, or based on the logistics of managing a large group of robots in hardware. This is further discussed in the following subsection. For this structure, we use 24 robots because this amount results in both full utilization of the swarm based on a simple partitioning of the structure into roughly equal voxel-count substructures, while also balancing against logistics challenges of handling larger robot swarms, which is further discussed in the following subsection.

4.0.3. Automated system throughput

The robotic system for the voxels is focused on being cheap and simple, and relies on parallelization to achieve improved throughput.

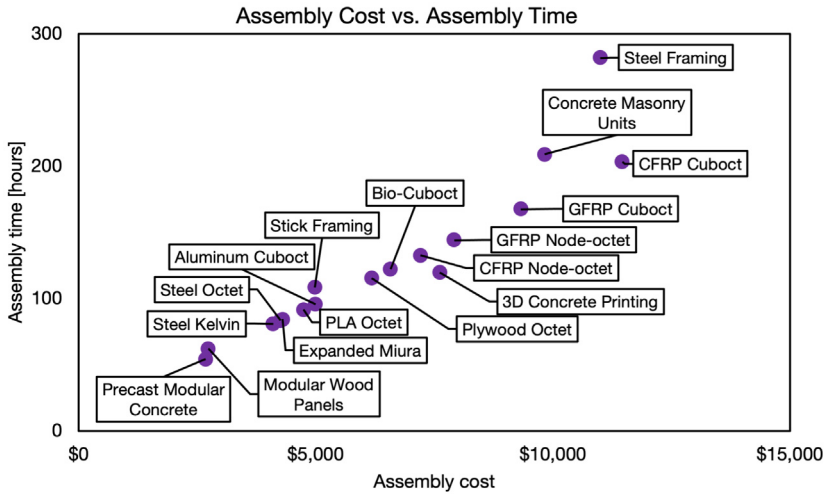

Fig. 18. Assembly cost versus the overall assembly time for every considered approach.

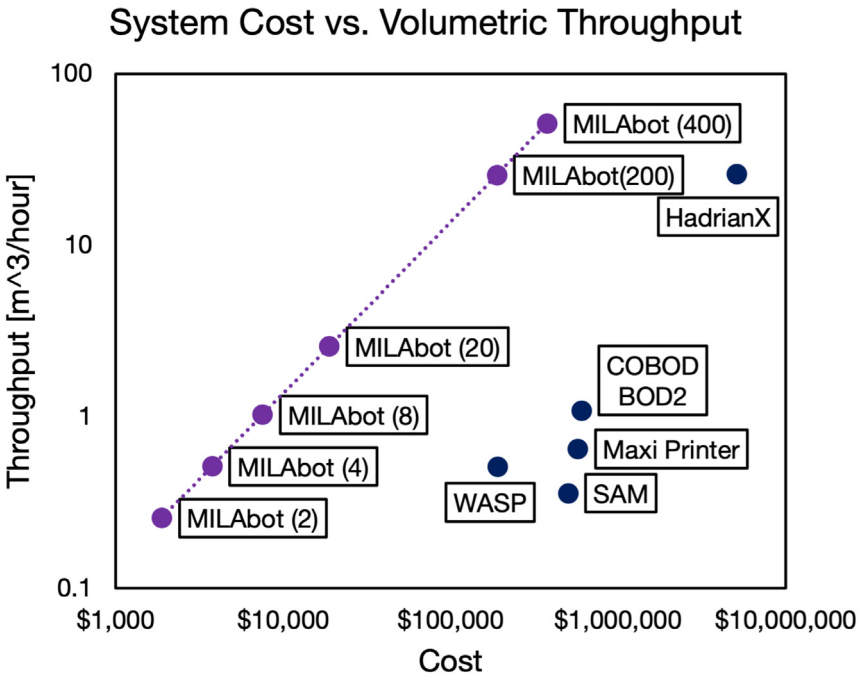

Fig. 19. System cost and volumetric assembly throughput scaling for increasing MILAbot swarm sizes as compared to selected existing automated concrete printing and bricklaying systems.

This stands in contrast to existing commercial approaches to automated structural building, which typically rely on expensive and large machines. In Fig. 19 we plot the volumetric throughput of the MILAbot system against some other existing systems: the WASP mud printer (gantry system) [26], the SAM bricklayer [33] (robot arm on a linear base), the Maxi concrete printer [86] (robot arm on a mobile base), the BOD2 concrete printer [80] (gantry system), and the Hadrian X bricklayer [34] (robotic arm on a crane with a mobile base). These prices are taken from the starting prices listed on each of these system's respective sites, while the MILAbot cost is doubled from the production cost.

A single MILAbot is much slower than the other approaches; however, it is also much cheaper. By increasing the amount of MILAbots, we linearly increase the throughput, and we catch up to (or exceed) the BOD2, Maxi, SAM, and WASP systems at less than 20 robots. While a swarm size of 20 voxel assemblers is larger than what has been previously demonstrated, it is still in a clearly tractable range, especially for well-partitioned builds. The MILAbot system catches up to the throughput of the HadrianX system at 200 robots at an order of magnitude cheaper. However, such a large swarm size, especially for a relatively small project, poses significant logistics and planning challenges that would limit our potential ability to trivially scale to those robot counts.

As previously stated, while increasing the robot count can increase system throughput, at some point, this will run into geometric, logistical, or computational barriers that prevent continued improvement, or could even begin reducing the system throughput. When these barriers come into play is highly geometry dependent, as the shape of the structure, as well as the access point around it on a site, can create bottlenecks for robotic assembly. If we consider the example of a long, solid and thin wall, if we are able to place robots and voxel feeds evenly along the length of it, we can achieve better than linear improvements in assembly throughput [87]. If we are however only able to place robots and voxel feeds at one end of the wall, we will receive little

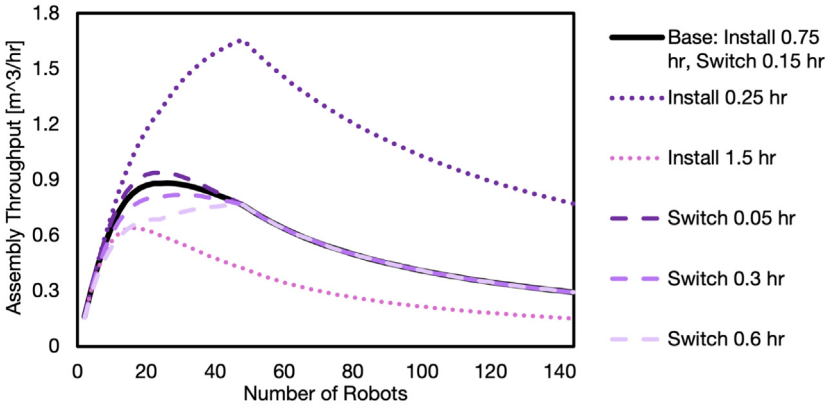

Fig. 20. Assembly throughput in meters cubed per hour versus the number of robots for the plywood voxel based simplified building.

to no benefit from adding further robots, as they will block each other along the path. Similarly, for roof structures or other overhangs, the quantity and size of their vertical supports dictates access for the robots. Although prior distributed robotic assembly work has demonstrated various strategies that can help mitigate this bottleneck effect, such as through bucket-brigade style behavior [88], our current path planning implementation does not accommodate this. Even if geometric constraints are not a limiting factor, the logistics of deploying large quantities of robots are relevant for real-world applications. That is, with a limited team of people to install and supervise the robots, increasing numbers of robots lead to increased installation and de-installation times. While this may be a less pronounced problem for more high autonomy operation, such as in-space assembly tasks, for the tasks considered here, these times can dominate over the robotic performance. Finally, because for this scenario we can precompute assembly paths, while computational challenges can eventually become limiting for very large structures, we are unlikely to encounter these for this system before running into the previously described physical barriers to scalability. Various literature has also explored alternate control systems for more highly autonomous and dense swarm systems [89].

To better see how these geometric and logistical challenges impact arbitrary scaling, we can consider our example structure, as built using the plywood voxel system. We used our digital twin software to simulate different partitions of this structure and how throughput is impacted by increasing robot quantities for these substructures. Based on our prior assumption of two workers monitoring the robot build, we factor in installation time as proportional to the quantity of robots used, assuming that two robots can be set up at a time. Our prior calculations also assume that the robots and voxel feeds can been manually moved around the build site as substructures are completed, as this enables the robots to fully access the sample structure without temporary supports. The time this takes is factored in based on how many (if any at all) robots need to be moved around on to continue assembling further substructures.

The assembly throughput in m^3/hr versus the number of robots for the plywood voxel building is plotted in Fig. 20, with a small parameter sweep of installation times and voxel feed switching times, to illustrate how these metrics impact overall throughput. The basic case is plotted in black, and assumes 0.75 h for every two robots to be installed, and 0.15 h for every two robots and voxel feeds to be moved to a new position. The alternate options vary only one of the parameters, as indicated by the legend. In the absence of the installation/deinstallation time considerations, throughput linearly increases until we reach the maximum amount of robots that can build without sharing a vertical stud, which is 48. At this point, the throughput continues increasing at a much slower rate, as each stud has enough capacity for two robots to split the assembly, improving the overall speed. However, because of the narrowness of certain sections of the horizontal joist elements, the additional robots are not able to contribute to building these. The throughput continues increasing until we start increasing the robot count to three per stud, at which point they begin to interfere with each other, resulting in a decrease in the assembly throughput. The addition of installation and switching time considerations primarily serves to penalize larger quantities of robots, pushing the peak productivity toward lower robot counts. While the timings for these actions are based around our experience with the hardware, these are highly approximate and would likely require deployment outside of a lab environment to more realistically evaluate. However, these results help to illustrate how physical constraints around building geometry and likely necessary manual actions during the assembly process can limit overall scalability.

The comparison to existing systems in Fig. 19 is intended to provide a simplified comparison point, as each of the considered systems face various limitations that impact both achievable assembly throughput and what types of geometry are buildable, making direct one-to-one comparison difficult. So, while Fig. 20 clearly indicates that for a structure of this size, we cannot arbitrarily scale into the hundreds of robots, a structure with 10 times the wall perimeter (which does not mean it needs to be an overall 10 times larger structure), could much more easily support an increased number of robots. This suggests that a potentially fruitful avenue of future work could be to consider both which types of structures are best suited for distributed robotic assembly as well as how overall structure designs might be modified to better accommodate robotic fabrication.

5. Limitations and future work

We evaluate voxel systems within a complete building-level comparison framework that considers embodied carbon, total cost, and assembly time, unlike prior voxel and architected lattice work, which focus primarily on mechanical characterization [12,59,60] or system demonstration outside of construction contexts [64,90]. While many prior robotic construction systems have been explored, these works often focus on demonstrating structural, robotic, or material performance [36,57,91] in isolation. Because our goal is to demonstrate the potential applicability of an entire material-robot system to building construction, a focus of this work is a normalized comparison of building approaches considering multiple metrics relevant to a construction system.

Similarly, much of the prior work on robotic construction emphasizes either structural performance or fabrication efficiency in isolation; here, we integrate structural simulation, robotic throughput modeling, and cradle-to-gate embodied carbon assessment under consistent boundary conditions. For comparability, all construction approaches,

including additive and modular systems, are normalized to equivalent functional requirements and levels of finish, enabling a more consistent evaluation of automation strategies in realistic building scenarios.

However, while this work demonstrates the potential of robotic voxel assembly as an efficient and sustainable in-situ construction approach, there are still substantial limitations that need to be addressed before this approach is ready for practical deployment. The voxel approaches have only been demonstrated at a lab scale, so many important performance characteristics, such as long term durability have not been evaluated.

We only consider the performance of the voxels in a basic mechanical loading scenario and we do not consider the stability of these structures under shearing or lateral loads. To fully validate the voxel system, not only would more substantial mechanical testing be required, but a slate of other properties would also need to be tested. In addition, we would need to evaluate the voxels for long-term use. For example, mechanical fatigue, thermal stresses from different material types, and humidity resistance may all negatively impact the performance of the voxel approaches over many years.

Significantly, the fire resistance of most of the considered voxel approaches, especially the FRP-based ones, is too low for use as structural elements in a building, and future research would need to address this. The fire performance is a major constraint especially for polymer-based voxel systems, and may prevent future use of these systems. For this reason, this study also evaluates steel and wood-based voxel systems whose intrinsic fire performance may be more compatible with conventional building codes, although it is important to note that the structure of these may make them more susceptible to fire damage. While intumescent coatings or mineral-filled composite formulations may improve behavior, such strategies would increase cost and embodied carbon and may not achieve required structural fire ratings. Future work should explicitly assess code-compliant configurations within the present LCA framework.

Our path-planning tools currently do not account for the physics of the system, which may be a significant limitation for structures such as these which have large cantilevers during the construction process. While some prior work has demonstrated integrated CAD and FEA for voxel systems [64], these do not incorporate robotic path-planning and are likely not suitable for simulating structures at the architectural scale, where total voxel counts are extremely high. Potential integration of other work [91,92] that has explored the generation of loading-aware robotic paths, or even hardware such as [93], which can measure loads in the structure, may be necessary for full scale deployment.

The robotic hardware system is also not at the requisite maturity yet for full-scale deployment, though there is active work towards this. The largest scale demonstrations of voxel assembly, from the MILAbot system, and from [13], both have limitations in the maneuvers that prevent efficient assembly of large structures, which is why, for this work, we simulate the performance using a vertically moving voxel feeder, which has not yet been demonstrated in hardware. Similarly, with the exception of the FFF-printed voxel, which is not a practical option, and the node-octet voxels, which have not been robotically assembled, all of the other voxels require some amount of assembly to go from 2D/2.5D faces into the voxel. In prior work, this has always been manual, but for real deployment, automating this would be necessary. Additionally, the delivery of voxels to the voxel feed or assembly robot is underexplored.

Based on the results from the assembly speed estimates, future work should also address more "complete" voxel modules. These voxels could potentially incorporate sheathing, insulation, or electrical or plumbing routing for a more direct-write assembly process. If this direction is further pursued, questions of how to properly seal a highly discretized structure become more relevant. Additionally, explorations of what the most appropriate size of voxel and size of robot may be relevant.

6. Conclusion

Depending on material and geometry selection, voxel-based systems were able to reduce the embodied carbon of the evaluated single-story building compared to concrete approaches. The plywood octet system demonstrated the lowest embodied carbon of the voxel approaches, with 17% the embodied carbon of the 3DCP approach, and 24% that of the precast concrete approach. The steel octet system had 36% the embodied carbon of 3DCP, and 52% that of precast, while slightly reducing the carbon footprint relative to the steel framing approach, at 91% the embodied carbon. On-site assembly time is competitive with existing approaches, at an average time of 99 h for the two voxel approaches, and an average of 155 h for the existing approaches, and the voxel systems are only outperformed by the large-panel based modular building systems. Total construction cost for the steel and plywood octet voxels is comparable to that of the concrete-based approaches, as well as the steel framing approach, although the stick-framing approach is substantially cheaper, at 70% and 63% the average cost of these other approaches, respectively.

This study shows that the robotic assembly of voxels has the potential to improve the sustainability and efficiency of construction compared to some existing construction approaches. For the voxel approaches, cost competitiveness depends on material selection and fabrication strategy. The voxel approach combines the mass-efficient benefits of framing systems with the automation benefits of 3DCP and modular prefabricated methods. Compared to the 3DCP approach, the voxel approach has lower embodied carbon, lower labor costs, and lower amortized equipment cost per structure, indicating the potential for discrete assembly in large-scale construction. Compared to modular prefabricated methods, such as prefabricated concrete systems or modular wood based systems, the voxel-based assembly approach is slower, but does not require large on-site infrastructure for installation and can support added geometric complexity without cost increases.

The results suggest that further exploring either a steel or wood voxel system would enable the most sustainability and cost benefits, and future work would focus on validating these projections with physical demonstrations. Future work could also explore where in the construction process adopting a discretized distributed robotic assembly system makes the most sense. The results demonstrate modular systems that leverage larger panels can achieve reasonable sustainability and cost metrics likely at an assembly speed that smaller voxel modules will not match. However, the ability to use smaller and simpler robots may have alternative benefits, especially toward more highly autonomous operation in remote or challenging environments, or towards creating reconfigurable or temporary structures.

As the work here explores a simplified single-story building, future work should also focus on projections for multi-story buildings or other large structures as a clearer path to scaling to large structures is one of the key motivators for exploring voxel-based systems. Scaling to multi-story structures will require evaluating metrics beyond mechanical performance, such as thermal expansion, fire safety, and relative humidity effects.

CRediT authorship contribution statement

Miana Smith: Writing – review & editing, Writing – original draft, Visualization, Methodology, Investigation, Formal analysis, Conceptualization. Paul Richard: Writing – review & editing, Software, Investigation. Alfonso Parra Rubio: Writing – review & editing, Writing – original draft, Investigation, Formal analysis. Neil Gershenfeld: Writing – review & editing, Supervision, Conceptualization.

Declaration of competing interest

The authors declare that they have no known competing financial interests or personal relationships that could have appeared to influence the work reported in this paper.

Acknowledgments

The authors thank Patricia Stathatou (Georgia Tech, School of Chemical & Biomolecular Engineering) and Caitlin Mueller (MIT, Civil and Environmental Engineering) for the helpful discussions and feedback on this work, and Anthony Pennes (MIT, Electrical Engineering and Computer Science) for fabrication assistance. This work was conducted in part at the Autodesk Seaport Innovation Center, and the authors would like to thank the team there for support and assistance. This work was supported by MIT Center for Bits and Atoms Consortia funding.

Appendix A. Voxel cost and emissions estimation methods

This section explains the methods and sources used to derive the cost and emissions estimates for the voxel approaches.

GFRP node connected octet (Fig. 1A) achieves a compressive modulus of 2.6 MPa at a density of 5.8 kg/m^3, while the CFRP node connected octet reaches a modulus of 7.97 MPa at the same density. The carbon intensity of these material systems is determined using the carbon intensity figures for PEI from [94], glass fiber from [95], or carbon fiber from [96], leading to an embodied carbon estimate of 12 kgCO_2e/kg for the GFRP version and 19 kgCO_2e/kg for the CFRP version. [60] provides the cost for each of these at $0.01 per cubic centimeter at $0.03 per cubic centimeter, respectively.

The GFRP cuboct (1B) has a compressive modulus of 3.2 MPa and a density of 32.5 kg/m^3 [66]. The CFRP cuboct (1C) has compressive modulus 1.1 MPa and density 10.1 kg/m^3 [13]. We use the embodied carbon estimate for nylon 66 from [97] and the prior GF and CF estimates, leading to a value of 5 kgCO_2e/kg for the GFRP lattice and 13 kgCO_2e/kg for the CFRP lattice. The cost of the GFRP lattice is $1.38 per face, excluding mold cost, while the CFRP lattice is $7.43 per face [13].

The bio-cuboct (1D) has a modulus of 9.39 MPa and a density of 73 kg/m^3. Based on the values reported in [14], the voxels have an embodied carbon equivalent of approximately 5 kgCO_2e/kg. Though this value is slightly higher than our estimate for the conventional GFRP voxel, the bio-cuboct has superior specific modulus performance. Because the material formulation for the bio-cuboct is discontinued, and because [14] does not provide a cost estimate, we re-use the cost per face from the [66] GFRP cuboct, which is likely a low estimate.

The reinforced Kelvin lattice (1F) has a modulus of 34 MPa and a density of 151 kg/m^3. It is worth noting that this lattice has a relatively smaller lattice pitch (17.2 mm) compared to the other considered approaches, and is designed for incrementally adding new faces of material as opposed to entire volumetric elements. However, for this work, we treat it as though it is also a voxel-based lattice decomposition. We estimate the embodied carbon of this approach by first estimating the embodied carbon of the mild steel sheet stock used to make the voxel parts. We start from the reported CO_2e emissions for producing hot-rolled merchant bar quality stock from Gerdau [98], which includes GHG emissions from initial steel production, and assume a cold-rolling finishing step consuming energy at rates described in [99] with an emissions factor based on the current Massachusetts grid embodied carbon per megawatt hour value of 418.666 kgCO_2e/MWh [100]. We then factor in the CO_2e emissions cost from cutting the material on a 1.2 kW laser cutter (xTool MetalFab), as well as the wasted material from the lattice cut pattern—for this shape, we estimated a maximum packing density of 23%. From this, we arrive at an embodied carbon estimate of 4 kgCO_2e/kg of produced voxel. We estimate the cost of the voxels to be $7 per kg of produced voxel based on the cost of sheet stock from [101] with the cost of electricity to cut the material and one technician paid at $25 per hour operating the machine for its entire run time.

The aluminum cuboct (Fig. 1G) is made directly from an aluminum substrate PCB (approximately 1.5 mm thick aluminum core with insulation, copper, and solder mask to a total 1.6 mm thickness) and reaches a modulus of 24 MPa at a density of 30.75 kg/m^3. We estimate the embodied carbon of this approach by combining the base embodied carbon associated with producing the aluminum at 11.8 kgCO_2e/kg, based on figures from [85], with the cost of producing a single layer PCB, which we estimate at 18.37 kgCO_2e/kg based on the figures in [102], leading to a value of 30.17 kgCO_2e/kg of produced voxel, the most carbon-intensive of the considered voxel approaches. The cost of this system is $0.35 per face, based on quotes from JLCPCB for 1000-part order quantities.

The expanded Miura (Fig. 1H) achieves a compressive modulus of 50 MPa at a density of 110 kg/m^3. We estimate the embodied carbon of this approach by combining the embodied carbon from producing the base materials with the additions from laminating the sandwich panel and processing it on a Zund flatbed cutter, determining the machine running cost with the same method as the laser cutter, assuming 67% packing efficiency. From this, we get 28 kgCO_2e/kg of produced voxel at a cost of $27.70 per kg.

The embodied carbon of the PLA octet (Fig. 1E) approach is based on the value provided in [103], with an overhead added based on printing the voxel on a Prusa Mk4 with an operator in attendance for 0.5% of the print time based on our measured print times versus print loading and unloading times. This results in a total embodied carbon of 3 kgCO_2e/kg. The cost is taken from the Prusa slicer, at $0.62 per voxel. The steel octet voxel embodied carbon is calculated in the same way as the Kelvin lattice, but with a maximum packing efficiency of 45%, resulting in 2.4 kgCO_2e/kg of produced voxel. We estimate the cost at $8 per kg of produced material. The plywood octet voxel is calculated similarly, starting with the emissions factor from [85], and processed with a 120 W CO_2e Epilog laser cutter, resulting in 1 kgCO_2e/kg of produced voxel, and a cost of $8 per kg of produced material.

Appendix B. FEA simulation and experimental validation

We recreated physical and virtual three-point bending tests to verify the analogy claimed in the paper: that the physical cellular materials we propose can be simulated as a digital continuum material. We selected the three-point bending test as it also challenges the material assumption in a more realistic way than a uniaxial compression test. A three point bending test is not fully tension dominated, but rather is a good combination of both compression and tension modes of work.

To this end, we selected three materials and four different beam architectures. Using the 3D printed edge-connected octet lattice, we produce two beams, one in PLA and another in a PLA/PHA blend. The compressive modulus of each is measured using a single unit cell specimen, and extrapolated as the bulk material property for simulation. We produced an additional beam using the node-connected octet lattice, but using a non-fiber reinforced Nylon. A 2 × 2 × 3 block sample was compressed to determine its compressive modulus and weighed to determine its weight. From the literature, [70] reports three-point bending test results for the geometry we evaluate in this paper, and these are taken as the experimental results for that beam. The dimensions of each beam we tested are listed in Table B.2.

We chose these geometries as they span a sweep of the voxel types evaluated in this paper. The PLA and PHA octet lattices leverage the compounded assembly, as previously described in this work, where pre-connected blocks (e.g. 1 × 3 strip of voxels) are assembled into larger structures primarily connected vertically through snap fit joints, with dove tail features providing additional lateral/tensile stability. The interleaving of the compounded blocks provides good structural stability and capacity to support bending loads. The node octet system then is connected voxel-by-voxel, and so is less likely to have joints with significantly different strengths and stiffnesses throughout. These voxels are connected via 0–80 screws and nuts. The expanded Miura voxel is a plate lattice system, and the beam assembly incorporates continuous sheets that are loaded under tension during bending, providing

Table B.2
Comparison of simulated and experimental 3-point bending tests.

	PLA Octet	PHA Octet	Expanded Miura	Nylon Node Octet
FEA stiffness (N/mm)	137	184	281	26
Measured stiffness (N/mm)	128	152	221	44
Compressive modulus (MPa)	15	25	45	1.5
Density (kg/m ^{3})	81	82	110	4.5
Lattice pitch (mm)	65	65	66	76.2
Beam dimensions (L×W×H)	6 × 1 × 2.5	10 × 2 × 6.5	8×1.5×2	8 × 2 × 3

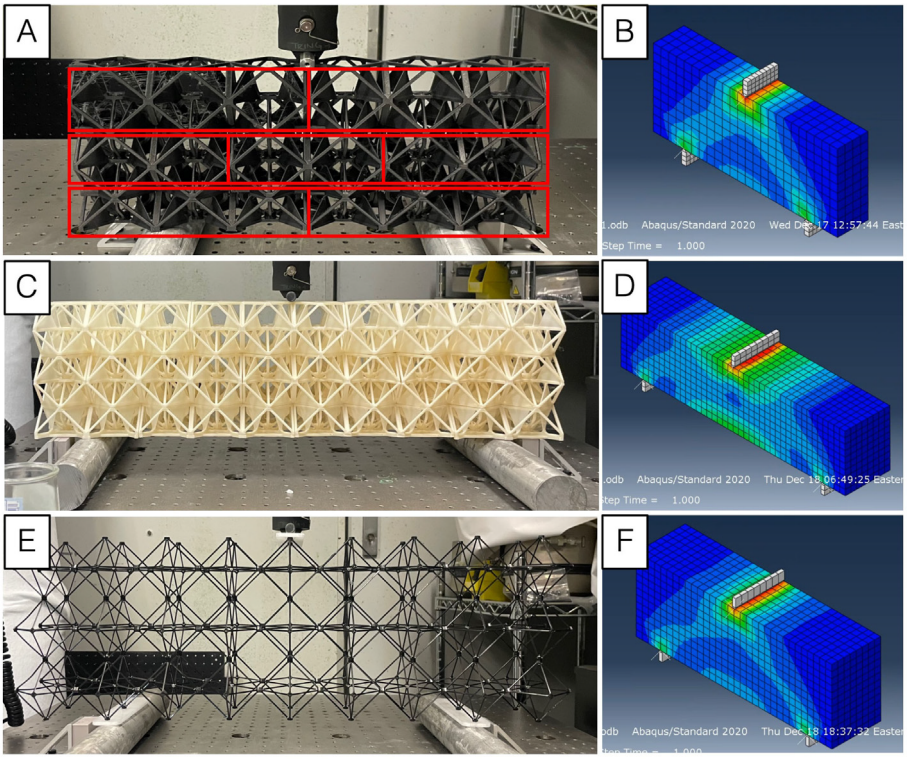

Fig. B.21. Three-point bending testing physical set up and simulated set up. A) The PLA octet beam, with separate voxel blocks highlighted in red. C) The PHA/PLA blend octet voxels. Like the PLA octet beam, this one also consists of stacked and staggered compounded voxel elements. E) The nylon node octet beam. B), D), F) are the simulated versions of the beam. A reference for the expanded Miura beam is available in [70].

a comparison point to a specimen with complete continuity. Voxels are connected via blind rivets.

In Abaqus, we model the three-point bending test by representing the specimen as a rectangular continuum with the corresponding elastic modulus E and Poisson's ratio ν, as specified in Table B.2. The cylindrical supports and the punch are modeled as discretely rigid bodies, assuming no deformation. The interactions are defined with tangential penalty friction using a coefficient of 0.15, and normal interaction is set as hard contact. A prescribed deflection is applied to the punch, and the resulting reaction forces are recorded to replicate the measurements obtained from the Instron load cell in the physical experiments. Displacement and reaction force data are extracted and compared with the experimental results. For all Abaqus simulations, units are defined as mm, N, and MPa (see Fig. B.21).

We see relatively good agreement between the simulated beam performance and the measured beam performance, in terms of the reaction force to displacement ratio. These are plotted in Fig. B.22. For the expanded Miura beam, the measured result is 221 N/mm while the simulated result is 281 N/mm. For the PLA octet beam, the measured result is 128 N/mm and the simulated result is 137 N/mm. For the PHA octet beam, the physical result is 221 N/mm and the simulated result 281 N/mm. For the nylon node octet, the physical result is 44 N/mm and the simulated result is 26 N/mm. This significant under performance of the FEA model is likely because of the softness of the bulk material, as the modulus is quite low. If we analytically calculate the expected bending stiffness EI based on our measured modulus, as well as the bending stiffness from our 3-point bending test, we see much closer results. Using this analytic bending stiffness EI, we predict a force–displacement ratio of 48 N/mm (this is plotted in Fig. B.22 as the dashed "beam" line). For all of these results, the physical behavior of the discretely assembled beam is relatively well aligned to that of the simulated continuum beam model. In addition to the existing literature on discrete lattice vs. continuum lattice performance, these results suggest that our simplified simulation model reasonably captures the real physical performance of voxel assemblies in more complex loading scenarios.

For both the structural archway and the three-point bending tests, the simulation code is available here: https://gitlab.cba.mit.edu/alfonso/abaqus-python-code-for-comparative-evaluation-of-da-lattices-for-construction/-/tree/main.

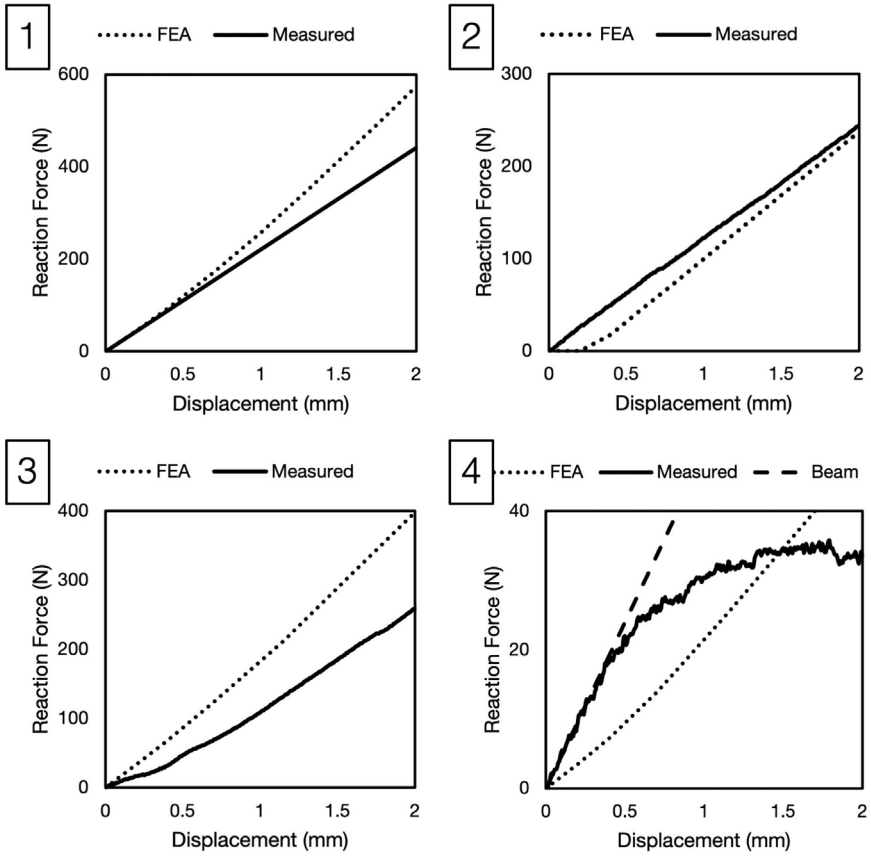

Fig. B.22. FEA and physical force–displacement plots for the four tested beams. (1) Expanded Miura beam. (2) PLA octet beam. (3) PLA/PHA octet beam. (4) Nylon node-octet beam. Note that for the Expanded Miura, the measured data is a plot of the slope of the raw data available from [70].

Table C.3
Comparison of building approaches with material, cost, and performance metrics.

Approach	Density (kg/m ^{3})	E (MPa)	Pitch (mm)	Voxels (#)	Wt. (kg)	EC (kgCO $_2$)	Mat. cost (USD)	Fab. cost (USD)	Total cost (USD)	Time (h)
Alum. Cuboct	30.8	24	150	10,416	1303	40,849	21,580	4991	26 571	95.8
GFRP Node-oct	5.8	2.6	76.2	267,720	1102	14,502	46,633	7917	54,551	144.4
CFRP Node-oct	5.8	8.0	76.2	226,776	627	13,622	111,090	7208	118,298	132.6
GFRP Cuboct	32.5	3.2	75	464,016	7150	34,688	2,758,734	9320	2,768,054	167.8
CFRP Cuboct	10.1	1.1	300	12,816	4097	56,367	325,129	11,458	336,587	203.3
Steel Kelvin	151	34	17.2	5,254,368	6044	28,259	841,48	4101	88,249	81.0
Bio-Cuboct	73	9.4	75	80,016	6552	34,306	1,381,008	6575	1,387,583	122.1
Exp. Miura	110	50	66	36,384	2402	23,024	70,590	4299	74,888	84.3
PLA Octet	82	25	65	44,328	3157	11,904	72,118	4741	76,859	91.6
Steel Octet	116	126	100	15,624	1921	6158	16,776	4252	21,028	83.5
Plywood Octet	15	8.1	100	69,624	1246	2874	13,301	6176	19,477	115.5
Steel Frame	–	–	–	–	2074	6609	15,859	10,999	26,858	282.1
Stick Frame	–	–	–	–	1150	1933	4983	4,981	9964	108.5
3D Concrete	–	–	–	–	46,267	17,338	12,973	7616	20,589	119.7
Precast Conc.	–	–	–	–	42,114	11,899	23,681	2677	26,358	54.3
CMU	–	–	–	–	48,022	14,005	14,250	9823	24,073	209.0

Appendix C. Key parameters of building approaches

The key parameters of the considered building approaches are summarized in Table C.3.

Data availability

Data will be made available on request.

References

[1] I. Agustí-Juan, G. Habert, Environmental design guidelines for digital fabrication, J. Clean. Prod. 142 (2017) 2780–2791, http://dx.doi.org/10.1016/j.jclepro.2016.10.190 , URL https://www.sciencedirect.com/science/article/pii/S0959652616318212 .

[2] Y.H. Dong, S.T. Ng, A modeling framework to evaluate sustainability of building construction based on LCSA, Int. J. Life Cycle Assess. 21 (4) (2016) 555–568, http://dx.doi.org/10.1007/s11367-016-1044-6 .

[3] M. Gebler, A.J.M. Schoot Uiterkamp, C. Visser, A global sustainability perspective on 3D printing technologies, Energy Policy 74 (2014) 158–167, http://

dx.doi.org/10.1016/j.enpol.2014.08.033 , URL https://www.sciencedirect.com/science/article/pii/S0301421514004868 .

[4] Y. Weng, M. Li, S. Ruan, T.N. Wong, M.J. Tan, K.L. Ow Yeong, S. Qian, Comparative economic, environmental and productivity assessment of a concrete bathroom unit fabricated through 3D printing and a precast approach, J. Clean. Prod. 261 (2020) 121245, http://dx.doi.org/10.1016/j.jclepro.2020.121245 , URL https://www.sciencedirect.com/science/article/pii/S0959652620312920 .

[5] T. Bock, The future of construction automation: Technological disruption and the upcoming ubiquity of robotics, Autom. Constr. 59 (2015) 113–121, http://dx.doi.org/10.1016/j.autcon.2015.07.022 , URL https://www.sciencedirect.com/science/article/pii/S092658051500165X .

[6] S.C. Joshi, A.A. Sheikh, 3D printing in aerospace and its long-term sustainability, Virtual Phys. Prototyp. 10 (4) (2015) 175–185, http://dx.doi.org/10.1080/17452759.2015.1111519 , Publisher: Taylor & Francis _eprint.

[7] Z. Zuo, W. De Corte, Y. Huang, X. Chen, Y. Zhang, J. Li, L. Zhang, J. Xiao, Y. Yuan, K. Zhang, L. Zhang, V. Mechtcherine, Propelling the widespread adoption of large-scale 3D printing, Nat. Rev. Mater. (2023) 1–3, http://dx.doi.org/10.1038/s41578-023-00626-1 , Publisher: Nature Publishing Group, URL https://www.nature.com/articles/s41578-023-00626-1 .

[8] N. Melenbrink, J. Werfel, A. Menges, On-site autonomous construction robots: Towards unsupervised building, Autom. Constr. 119 (2020) 103312, http://dx.doi.org/10.1016/j.autcon.2020.103312 , URL https://www.sciencedirect.com/science/article/pii/S0926580520301746 .

[9] N. Zhang, J. Sanjayan, Concrete 3D printing and digital fabrication technologies for bridge construction, Autom. Constr. 179 (2025) 106485, http://dx.doi.org/10.1016/j.autcon.2025.106485 , URL https://www.sciencedirect.com/science/article/pii/S0926580525005254 .

[10] H.J. Wagner, M. Alvarez, O. Kyjanek, Z. Bhiri, M. Buck, A. Menges, Flexible and transportable robotic timber construction platform – TIM, Autom. Constr. 120 (2020) 103400, http://dx.doi.org/10.1016/j.autcon.2020.103400 , URL https://www.sciencedirect.com/science/article/pii/S0926580520309808 .

[11] T.A. Schaedler, W.B. Carter, Architected cellular materials, Annu. Rev. Mater. Res. 46 (1) (2016) 187–210, http://dx.doi.org/10.1146/annurev-matsci-070115-031624 , _eprint:.

[12] K.C. Cheung, N. Gershenfeld, Reversibly assembled cellular composite materials, Science 341 (6151) (2013) 1219–1221, http://dx.doi.org/10.1126/science.1240889 , URL https://www.science.org/doi/10.1126/science.1240889 .

[13] C.E. Gregg, D. Catanoso, O.I.B. Formoso, I. Kostitsyna, M.E. Ochalek, T.J. Olatunde, I.W. Park, F.M. Sebastianelli, E.M. Taylor, G.T. Trinh, K.C. Cheung, Ultralight, strong, and self-reprogrammable mechanical metamaterials, Sci. Robot. 9 (86) (2024) eadi2746, http://dx.doi.org/10.1126/scirobotics.adi2746 , Publisher: American Association for the Advancement of Science, URL https://www.science.org/doi/10.1126/scirobotics.adi2746 .

[14] D. Georgiou, D. Okegbu, Z. Yang, T. Wang, M.R. Snowdon, A. Mohanty, N. Gershenfeld, W. Yan, C.E. Athanasiou, Eco-voxels: Building blocks for sustainable, load-bearing structures, Matter 8 (7) (2025) 102106, http://dx.doi.org/10.1016/j.matt.2025.102106 , URL https://www.sciencedirect.com/science/article/pii/S2590238525001493 .

[15] J. Liu, V. Nguyen-Van, B. Panda, K. Fox, A. du Plessis, P. Tran, Additive manufacturing of sustainable construction materials and form-finding structures: A review on recent progresses, 3D Print. Addit. Manuf. 9 (1) (2022) 12–34, http://dx.doi.org/10.1089/3dp.2020.0331 , Publisher: Mary Ann Liebert, Inc., publishers, URL https://www.liebertpub.com/doi/10.1089/3dp.2020.0331 .

[16] B. Drieth, Hannah begins construction on "first multi-storey 3D-printed house in the US", 2022, Section: Architecture, URL https://www.dezeen.com/2022/10/04/hannah-multi-storey-3d-printed-home-houston/ ,

[17] M.-C. Florian, ICON reveals new 3D-printed residential development in Wimberley, Texas | ArchDaily, 2024, URL https://www.archdaily.com/1018953/icon-reveals-new-3d-printed-residential-development-in-wimberley-texas .

[18] H. Abdalla, K.P. Fattah, M. Abdallah, A.K. Tamimi, Environmental footprint and economics of a full-scale 3D-printed house, Sustainability 13 (21) (2021) 11978, http://dx.doi.org/10.3390/su132111978 , Number: 21 Publisher: Multidisciplinary Digital Publishing Institute, URL https://www.mdpi.com/2071-1050/13/21/11978 .

[19] M. Batikha, R. Jotangia, M.Y. Baaj, I. Mousleh, 3D concrete printing for sustainable and economical construction: A comparative study, Autom. Constr. 134 (2022) 104087, http://dx.doi.org/10.1016/j.autcon.2021.104087 , URL https://www.sciencedirect.com/science/article/pii/S0926580521005380 .

[20] A. Jipa, B. Dillenburger, 3D printed formwork for concrete: State-of-the-art, opportunities, challenges, and applications, 3D Print. Addit. Manuf. 9 (2) (2022) 84–107, http://dx.doi.org/10.1089/3dp.2021.0024 , Publisher: Mary Ann Liebert, Inc., publishers, URL https://www.liebertpub.com/doi/10.1089/3dp.2021.0024 .

[21] N.D. Bello, A.M. Memari, Comparative review of the technology and case studies of 3D concrete printing of buildings by several companies, Buildings 13 (1) (2023) 106, http://dx.doi.org/10.3390/buildings13010106 , Publisher: Multidisciplinary Digital Publishing Institute, URL https://www.mdpi.com/2075-5309/13/1/106 .

[22] A. Curth, N. Pearl, A. Castro-Salazar, C. Mueller, L. Sass, 3D printing earth: Local, circular material processing, fabrication methods, and life cycle assessment, Constr. Build. Mater. 421 (2024) 135714, http://dx.doi.org/10.1016/j.conbuildmat.2024.135714 , URL https://www.sciencedirect.com/science/article/pii/S0950061824008559 .

[23] M. Sonebi, Y. Ammar, P. Diederich, 15 - Sustainability of cement, concrete and cement replacement materials in construction, in: J.M. Khatib (Ed.), Sustainability of Construction Materials, second ed., in: Woodhead Publishing Series in Civil and Structural Engineering, Woodhead Publishing, 2016, pp. 371–396, http://dx.doi.org/10.1016/B978-0-08-100370-1.00015-9 , URL https://www.sciencedirect.com/science/article/pii/B9780081003701000159 .

[24] V.N. Nerella, M. Krause, V. Mechtcherine, Direct printing test for buildability of 3D-printable concrete considering economic viability, Autom. Constr. 109 (2020) 102986, http://dx.doi.org/10.1016/j.autcon.2019.102986 , URL https://www.sciencedirect.com/science/article/pii/S0926580518308343 .

[25] T. Marchment, J. Sanjayan, Mesh reinforcing method for 3D concrete printing, Autom. Constr. 109 (2020) 102992, http://dx.doi.org/10.1016/j.autcon.2019.102992 , URL https://www.sciencedirect.com/science/article/pii/S0926580519306132 .

[26] 3D printer house | crane WASP, 2025, URL https://www.3dwasp.com/en/3d-printer-house-crane-wasp/ ,

[27] First 100% bio-based 3D-printed home unveiled at the University of Maine - umaine news - University of Maine, 2022, URL https://umaine.edu/news/blog/2022/11/21/first-100-bio-based-3d-printed-home-unveiled-at-the-university-of-maine/ .

[28] Polymaker, Polymaker's "liuyun bridge" - polymaker, 2021, URL https://polymaker.com/polymakers-liuyun-bridge/ .

[29] Branch technology, 2024, URL https://branchtechnology.com/ ,

[30] MX3D | bridge, 2024, URL https://mx3d.com/industries/mx3d-bridge/ .

[31] 3D printed rocket launched using innovative NASA alloy - NASA, 2023, Section: Marshall Space Flight Center, URL https://www.nasa.gov/centers-and-facilities/marshall/3d-printed-rocket-launched-using-innovative-nasa-alloy/ .

[32] M. Li, D. Li, J. Zhang, J.C. Cheng, V.J. Gan, 3D printing in modular construction: Opportunities and challenges, in: International conference on construction engineering and project management, Korea Institute of Construction Engineering and Management, 2020, pp. 75–84, http://dx.doi.org/10.6106/ICCEPM.2020.0075 .

[33] SAM, 2024, URL https://www.construction-robotics.com/sam-2/ ,

[34] Hadrian x® | outdoor construction & bricklaying robot from FBR, 2025, URL https://www.fbr.com.au/view/hadrian-x .

[35] P. Eversmann, J. Ochs, J. Heise, Z. Akbar, S. Böhm, Additive timber manufacturing: A novel, wood-based filament and its additive robotic fabrication techniques for large-scale, material-efficient construction, 3D Print. Addit. Manuf. 9 (3) (2022) 161–176, http://dx.doi.org/10.1089/3dp.2020.0356 , Publisher: Mary Ann Liebert, Inc., publishers, URL https://www.liebertpub.com/doi/10.1089/3dp.2020.0356 .

[36] A. Menges, B. Sheil, R. Glynn, M. Skavara, Fabricate 2017, UCL Press, 2017, http://dx.doi.org/10.2307/j.ctt1n7qkg7 , URL http://www.jstor.org/stable/10.2307/j.ctt1n7qkg7 .

[37] House of design, 2024, URL https://thehouseofdesign.com/ .

[38] S. Bodea, P. Mindermann, G.T. Gresser, A. Menges, Additive manufacturing of large coreless filament wound composite elements for building construction, 3D Print. Addit. Manuf. 9 (3) (2022) 145–160, http://dx.doi.org/10.1089/3dp.2020.0346 , Publisher: Mary Ann Liebert, Inc., publishers, URL https://www.liebertpub.com/doi/10.1089/3dp.2020.0346 .

[39] X. Zhang, M. Li, J.H. Lim, Y. Weng, Y.W.D. Tay, H. Pham, Q.-C. Pham, Large-scale 3D printing by a team of mobile robots, Autom. Constr. 95 (2018) 98–106, http://dx.doi.org/10.1016/j.autcon.2018.08.004 , URL https://linkinghub.elsevier.com/retrieve/pii/S0926580518304011 .

[40] A. Chourasia, S. Singhal, null Manivannan, Prefabricated volumetric modular construction: A review on current systems, challenges, and future prospects, Pr. Period. Struct. Des. Constr. 28 (1) (2023) 03122009, http://dx.doi.org/10.1061/PPSCFX.SCENG-1185 , arXiv:https://ascelibrary.org/doi/pdf/10.1061/PPSCFX.SCENG-1185 , URL https://ascelibrary.org/doi/abs/10.1061/PPSCFX.SCENG-1185 .

[41] Precast/Prestressed Concrete Institute, PCI Design Handbook Precast and Prestressed Concrete, fifth ed., Precast/Prestressed Concrete Institute, 1999, URL https://normanray.wordpress.com/wp-content/uploads/2011/03/pci_design_handbook_5th-ed_precast-prestressed-concrete.pdf.

[42] Tilt-Up Concrete Association, Construction basics, 2025, https://tilt-up.org/construction/basics/ . (Accessed 20 December 2025).

[43] Insulating Concrete Forms Manufacturers Association, Insulating concrete forms manufacturers association, 2025, https://icf-ma.org/ . (Accessed 20 December 2025).

[44] Y. Mugahed Amran, M. El-Zeadani, Y. Huei Lee, Y. Yong Lee, G. Murali, R. Feduik, Design innovation, efficiency and applications of structural insulated panels: A review, Structures 27 (2020) 1358–1379, http://dx.doi.org/10.1016/j.istruc.2020.07.044 , URL https://www.sciencedirect.com/science/article/pii/S235201242030357X .

[45] A.P.R. Lauer, E. Benner, T. Stark, S. Klassen, S. Abolhasani, L. Schroth, A. Gienger, H.J. Wagner, V. Schwieger, A. Menges, O. Sawodny, Automated on-site assembly of timber buildings on the example of a biomimetic shell, Autom. Constr. 156 (2023) 105118, http://dx.doi.org/10.1016/j.autcon.2023.105118 , URL https://www.sciencedirect.com/science/article/pii/S0926580523003783 .

[46] N. Opgenorth, D.N. Locatelli, S. Leder, H.J. Wagner, A. Menges, Multi-scalar robotic fabrication system for on-site press gluing in multi-storey timber buildings, Autom. Constr. 168 (2024) 105774, http://dx.doi.org/10.1016/j.autcon.2024.105774 , URL https://www.sciencedirect.com/science/article/pii/S0926580524005107 .

[47] Built Robotics, Inc., Built robotics — Robots that build the world, 2025, https://www.builtrobotics.com/ . (Accessed 20 December 2025).

[48] Canvas, Canvas 1200cx: The world's first compact drywall robot, 2025, https://canvas.build/products/canvas1200cx/ . (Accessed 20 December 2025).

[49] K.H. Petersen, N. Napp, R. Stuart-Smith, D. Rus, M. Kovac, A review of collective robotic construction, Sci. Robot. 4 (28) (2019) eaau8479, http://dx.doi.org/10.1126/scirobotics.aau8479 , Publisher: American Association for the Advancement of Science, URL https://www.science.org/doi/10.1126/scirobotics.aau8479 .

[50] F. Augugliaro, S. Lupashin, M. Hamer, C. Male, M. Hehn, M.W. Mueller, J.S. Willmann, F. Gramazio, M. Kohler, R. D'Andrea, The flight assembled architecture installation: Cooperative construction with flying machines, IEEE Control Syst. Mag. 34 (4) (2014) 46–64, http://dx.doi.org/10.1109/MCS.2014.2320359 , Conference Name: IEEE Control Systems Magazine, URL https://ieeexplore.ieee.org/document/6853477?arnumber=6853477 .

[51] A. Mirjan, F. Augugliaro, R. D'Andrea, F. Gramazio, M. Kohler, Building a bridge with flying robots, in: D. Reinhardt, R. Saunders, J. Burry (Eds.), Robotic Fabrication in Architecture, Art and Design 2016, Springer International Publishing, 2016, pp. 34–47, http://dx.doi.org/10.1007/978-3-319-26378-6_3 , URL http://link.springer.com/10.1007/978-3-319-26378-6_3 .

[52] S. Goessens, C. Mueller, P. Latteur, Feasibility study for drone-based masonry construction of real-scale structures, Autom. Constr. 94 (2018) 458–480, http://dx.doi.org/10.1016/j.autcon.2018.06.015 , URL https://www.sciencedirect.com/science/article/pii/S0926580518301961 .

[53] K. Petersen, R. Nagpal, J. Werfel, TERMES: An autonomous robotic system for three-dimensional collective construction, Robot.: Sci. Syst. (2011).

[54] A. Hsu, A. Wong-Foy, B. McCoy, C. Cowan, J. Marlow, B. Chavez, T. Kobayashi, D. Shockey, R. Pelrine, Application of micro-robots for building carbon fiber trusses, in: 2016 International Conference on Manipulation, Automation and Robotics At Small Scales, MARSS, 2016, pp. 1–6, http://dx.doi.org/10.1109/MARSS.2016.7561729 .

[55] S. Leder, H. Kim, O.S. Oguz, N. Kubail Kalousdian, V.N. Hartmann, A. Menges, M. Toussaint, M. Sitti, Leveraging building material as part of the in-plane robotic kinematic system for collective construction, Adv. Sci. 9 (24) (2022) 2201524, http://dx.doi.org/10.1002/advs.202201524 , _eprint: https://onlinelibrary.wiley.com/doi/pdf/10.1002/advs.202201524 , URL https://onlinelibrary.wiley.com/doi/abs/10.1002/advs.202201524 .

[56] L. Siriwardena, T. Stark, S. Lut, H.J. Wagner, M. Maierhofer, S. Bechert, J. Knippers, A. Menges, Joint effort - a material-robot system for fibrous joints of lightweight timber construction, in: Proceedings of the 9th ACM Symposium on Computational Fabrication, SCF '24, Association for Computing Machinery, New York, NY, USA, 2024, http://dx.doi.org/10.1145/3639473.3665791 , URL https://doi.org/10.1145/3639473.3665791 .

[57] P.Y. Leung, A.A. Apolinarska, D. Tanadini, F. Gramazio, M. Kohler, Automatic assembly of jointed timber structure using distributed robotic clamps, in: PROJECTIONS: Proceedings of the 26th International Conference of the Association for Computer-Aided Architectural Design, vol. 1, Association for Computer Aided Architectural Design Research in Asia, 2021, pp. 583–592, http://dx.doi.org/10.52842/conf.caadria.2021.1.583 .

[58] M. Smith, A. Abdel-Rahman, N. Gershenfeld, Self-reconfigurable robots for collaborative discrete lattice assembly, in: 2024 IEEE International Conference on Robotics and Automation, ICRA, 2024, pp. 3624–3631, http://dx.doi.org/10.1109/ICRA57147.2024.10609866 , URL https://ieeexplore.ieee.org/document/10609866 .

[59] X. Zheng, H. Lee, T.H. Weisgraber, M. Shusteff, J. DeOtte, E.B. Duoss, J.D. Kuntz, M.M. Biener, Q. Ge, J.A. Jackson, S.O. Kucheyev, N.X. Fang, C.M. Spadaccini, Ultralight, ultrastiff mechanical metamaterials, Science 344 (6190) (2014) 1373–1377, http://dx.doi.org/10.1126/science.1252291 , Publisher: American Association for the Advancement of Science, URL https://www.science.org/doi/10.1126/science.1252291 .

[60] C.E. Gregg, J.H. Kim, K.C. Cheung, Ultra-light and scalable composite lattice materials, Adv. Eng. Mater. 20 (9) (2018) 1800213, http://dx.doi.org/10.1002/adem.201800213 , _eprint: https://onlinelibrary.wiley.com/doi/pdf/10.1002/adem.201800213 , URL https://onlinelibrary.wiley.com/doi/abs/10.1002/adem.201800213 .

[61] T.A. Schaedler, A.J. Jacobsen, A. Torrents, A.E. Sorensen, J. Lian, J.R. Greer, L. Valdevit, W.B. Carter, Ultralight metallic microlattices, Science 334 (6058) (2011) 962–965, http://dx.doi.org/10.1126/science.1211649 , URL https://www.science.org/doi/10.1126/science.1211649 .

[62] B. Jenett, N. Gershenfeld, P. Guerrier, Building block-based assembly of scalable metallic lattices, in: Volume 4: Processes, American Society of Mechanical Engineers, College Station, Texas, USA, 2018, http://dx.doi.org/10.1115/MSEC2018-6442 , V004T03A053.

[63] B. Jenett, D. Cellucci, K. Cheung, C. Gregg, Meso-scale digital materials: Modular, reconfigurable, lattice-based structures, in: Proceedings of the 2016 Manufacturing Science and Engineering Conference (MSEC2016), ASME, Virginia Tech, Blacksburg, USA, 2016, Paper MSEC2016-8767. Accessed at https://cba.mit.edu/docs/papers/16.07.msec.bridge.pdf .

[64] M. Smith, J. Forman, A. Abdel-Rahman, S. Wang, N. Gershenfeld, Voxel invention kit: Reconfigurable building blocks for prototyping interactive electronic structures, in: Proceedings of the 2025 CHI Conference on Human Factors in Computing Systems, CHI '25, Association for Computing Machinery, New York, NY, USA, 2025, pp. 1–15, http://dx.doi.org/10.1145/3706598.3713948 , URL https://dl.acm.org/doi/10.1145/3706598.3713948 .

[65] N.B. Cramer, D.W. Cellucci, O.B. Formoso, C.E. Gregg, B.E. Jenett, J.H. Kim, M. Lendraitis, S.S. Swei, G.T. Trinh, K.V. Trinh, K.C. Cheung, Elastic shape morphing of ultralight structures by programmable assembly, Smart Mater. Struct. 28 (5) (2019) 055006, http://dx.doi.org/10.1088/1361-665X/ab0ea2 .

[66] B. Jenett, C. Cameron, F. Tourlomousis, A.P. Rubio, M. Ochalek, N. Gershenfeld, Discretely assembled mechanical metamaterials, Sci. Adv. 6 (47) (2020) http://dx.doi.org/10.1126/sciadv.abc9943 , URL https://www.science.org/doi/10.1126/sciadv.abc9943 .

[67] B. Jenett, K. Cheung, C. Gregg, D.W. Cellucci, Design of multifunctional hierarchical space structures, in: 2017 IEEE Aerospace Conference, IEEE, Big Sky, MT, USA, 2017, http://dx.doi.org/10.1109/AERO.2017.7943913 , NASA Document ID 20180007137. Accessed from https://ntrs.nasa.gov/api/citations/20180007137/downloads/20180007137.pdf .

[68] B. Jenett, A. Abdel-Rahman, K. Cheung, N. Gershenfeld, Material–robot system for assembly of discrete cellular structures, IEEE Robot. Autom. Lett. 4 (4) (2019) 4019–4026, http://dx.doi.org/10.1109/LRA.2019.2930486 , URL https://ieeexplore.ieee.org/document/8769886/ .

[69] S. Keating, N.A. Spielberg, J. Klein, N. Oxman, Digital construction platform: A compound arm approach, Keating (2014) Accepted: 2014-11-14T16:50:10Z ISBN: 9783319046624 Publisher: Springer-Verlag, URL https://dspace.mit.edu/handle/1721.1/91574 .

[70] A. Parra Rubio, K. Mundilova, D. Preiss, E.D. Demaine, N. Gershenfeld, Kirigami corrugations: Strong, modular, and programmable plate lattices, in: Volume 8: 47th Mechanisms and Robotics Conference, MR, in: International Design Engineering Technical Conferences and Computers and Information in Engineering Conference, 2023, http://dx.doi.org/10.1115/DETC2023-116481 .

[71] H.G. Bhundiya, Z.C. Cordero, Bend-forming: A CNC deformation process for fabricating 3D wireframe structures, Addit. Manuf. Lett. 6 (2023) 100146, http://dx.doi.org/10.1016/j.addlet.2023.100146 , URL https://www.sciencedirect.com/science/article/pii/S2772369023000270 .

[72] Z. Xu, A.M. Dollar, Chain-based lattice printing for efficient robotically-assembled structures, Commun. Eng. 3 (2024) 157, http://dx.doi.org/10.1038/s44172-024-00305-1 .

[73] Tetmet SAS, Adaptive spatial lattice manufacturing (ASLM), 2025, https://www.tetmet.net/aslm . (Accessed 29 December 2025).

[74] M. Smith, P. Richard, A. Kyaw, N. Gershenfeld, Hierarchical discrete lattice assembly: An approach for the digital fabrication of scalable macroscale structures, in: ACM Symposium on Computational Fabrication, SCF'25, ACM, New York, NY, USA, 2025, p. 15, http://dx.doi.org/10.1145/3745778.3766665 .

[75] M.E. Carney, Discrete Cellular Lattice Assembly (Ph.D. thesis), Massachusetts Institute of Technology, Cambridge MA, 2015, URL https://cba.mit.edu/docs/theses/15.09.Carney.pdf .

[76] American Society of Civil Engineers (Ed.), Minimum design loads for buildings and other structures, 2. print, in: ASCE standard ASCE/SEI, (7–10) ASCE, American Society of Civil Engineers, Reston, Va, 2011, http://dx.doi.org/10.1061/9780784412916 .

[77] ICC, 2018 International Building Code (IBC), ICC, 2018, URL https://codes.iccsafe.org/content/IBC2018/chapter-16-structural-design .

[78] RSMeans Gordian, RSMeans data online, 2018, URL https://www.rsmeansonline.com/SearchData .

[79] M. Mohammad, E. Masad, S.G. Al-Ghamdi, 3D concrete printing sustainability: A comparative life cycle assessment of four construction method scenarios, Buildings 10 (12) (2020) 245, http://dx.doi.org/10.3390/buildings10120245 , Publisher: Multidisciplinary Digital Publishing Institute, URL https://www.mdpi.com/2075-5309/10/12/245 .

[80] COBOD, EU COBOD BOD2 tech specs, 2022, URL https://cobod.com/wp-content/uploads/2022/06/eu-cobod-bod2-techspecs.pdf .

[81] P.C. on Precast Sandwich Wall Panels, Sandwich Wall Panels Guide, Tech. rep., Precast/Prestressed Concrete Institute, 1997, URL https://www.pci.org/PCI_Docs/Design_Resources/Misc/Sandwich%20Wall%20Panels%20Guide.pdf .

[82] ClarkDietrich, 600S162-54-p (50ksi, CP60, punched), 2025, URL https://www.itools.clarkdietrich.com/submittalpro/dyn_pdf/%7B%22pdf_type%22%3A%22individual_product%22%2C%22project_product_code%22%3A%22product%7Cstructural_stud~product_code%7C600S162-54-P~coating%7CCP60~punched%7CP%22%7D/CD_600S162-54-P.pdf .

[83] ISO, Environmental management – Life cycle assessment – Principles and framework, Tech. Rep. ISO 14040:2021, International Organization for Standardization, Geneva, Switzerland, 2021.
[84] ISO, Environmental Management – Life Cycle Assessment – Requirements and Guidelines, Tech. Rep. ISO 14044:2021, International Organization for Standardization, Geneva, Switzerland, 2021.
[85] B. Waldman, A. Hyatt, S. Carlisle, J. Palmeri, K. Simonen, 2023 Carbon Leadership Forum North American Material Baselines (Version 2), Tech. rep., Carbon Leadership Forum, University of Washington, Seattle, WA, 2023, URL http://hdl.handle.net/1773/49965 .
[86] MaxiPrinter | concrete 3D printer | constructions-3D, 2025, URL https://www.constructions-3d.com/en/maxiprinter .
[87] A. Abdel-Rahman, C. Cameron, B. Jenett, M. Smith, N. Gershenfeld, Self-replicating hierarchical modular robotic swarms, Commun. Eng. 1 (1) (2022) 35, http://dx.doi.org/10.1038/s44172-022-00034-3 , URL https://www.nature.com/articles/s44172-022-00034-3 .
[88] J. Garcia, M. Yannuzzi, P. Kramer, C. Rieck, S.P. Fekete, A.T. Becker, Reconfiguration of a 2D structure using spatio-temporal planning and load transferring, in: 2024 IEEE International Conference on Robotics and Automation, ICRA, 2024, pp. 8735–8741, http://dx.doi.org/10.1109/ICRA57147.2024.10611057 , URL https://ieeexplore.ieee.org/document/10611057/?arnumber=10611057 .
[89] H. Hamann, Swarm Robotics: A Formal Approach, first ed., Springer, Cham, 2018, http://dx.doi.org/10.1007/978-3-319-74528-2 .
[90] B. Jenett, S. Calisch, D. Cellucci, N. Cramer, N. Gershenfeld, S. Swei, K.C. Cheung, Digital morphing wing: Active wing shaping concept using composite lattice-based cellular structures, Soft Robot. 4 (1) (2017) 33–48, http://dx.doi.org/10.1089/soro.2016.0032 , Publisher: Mary Ann Liebert, Inc., publishers, URL https://www.liebertpub.com/doi/10.1089/soro.2016.0032 .
[91] Y. Huang, J.V. Carstensen, C.T. Mueller, 3D truss topology optimization for automated robotic spatial extrusion, in: Proceedings of the IASS Symposium, International Association for Shell and Spatial Structures, Boston, USA, 2018, URL https://www.ingentaconnect.com/content/iass/piass/2018/00002018/00000019/art00017 .
[92] Y. Huang, C. Garrett, C. Mueller, Constructability-driven design of frame structures with state-space search methods, Autom. Constr. 167 (2024) 105711, http://dx.doi.org/10.1016/j.autcon.2024.105711 , URL https://www.sciencedirect.com/science/article/pii/S0926580524004473 .
[93] N. Melenbrink, P. Kassabian, A. Menges, J. Werfel, Towards force-aware robot collectives for on-site construction, 2017, http://dx.doi.org/10.52842/conf.acadia.2017.382 .
[94] M. Bachmann, A. Marxen, R. Schomäcker, A. Bardow, High performance, but low cost and environmental impact? Integrated techno-economic and life cycle assessment of polyoxazolidinone as a novel high-performance polymer, Green Chem. 24 (23) (2022) 9143–9156, http://dx.doi.org/10.1039/D2GC02400D , Publisher: Royal Society of Chemistry, URL https://pubs.rsc.org/en/content/articlelanding/2022/gc/d2gc02400d .
[95] EPA, 2019 fiberglass plant carbon intensities fact sheet .pdf, 2019, URL https://www.epa.gov/system/files/documents/2022-06/2019%20Fiberglass%20Plant%20Carbon%20Intensities%20Fact%20Sheet%20.pdf ,
[96] K. Kawajiri, K. Sakamoto, Environmental impact of carbon fibers fabricated by an innovative manufacturing process on life cycle greenhouse gas emissions, Sustain. Mater. Technol. 31 (2022) e00365, http://dx.doi.org/10.1016/j.susmat.2021.e00365 , URL https://www.sciencedirect.com/science/article/pii/S2214993721001202 .
[97] S.R. Nicholson, N.A. Rorrer, A.C. Carpenter, G.T. Beckham, Manufacturing energy and greenhouse gas emissions associated with plastics consumption, Joule 5 (3) (2021) 673–686, http://dx.doi.org/10.1016/j.joule.2020.12.027 , URL https://www.sciencedirect.com/science/article/pii/S2542435120306267 .
[98] G. S/A, EPD MBQ gerdau cambridge, 2025, URL https://www2.gerdau.com/sites/gln_gerdau/files/downloadable_files/EPD%20MBQ%20Gerdau%20Cambridge.pdf ,
[99] L. Price, G. Phylipsen, E. Worrell, Energy use and carbon dioxide emissions in the steel sector in key developing countries, Tech. Rep. LBNL–46987, 783473, OSTI, 2001, pp. LBNL–46987, 783473, http://dx.doi.org/10.2172/783473 , URL http://www.osti.gov/servlets/purl/783473-fcGKaj/webviewable/ .
[100] Massachusetts electricity profile 2023, 2023, URL https://www.eia.gov/electricity/state/massachusetts/ .
[101] MetalsDepot® - buy steel sheet online - any quantity, any size!, 2025, URL https://www.metalsdepot.com/steel-products/steel-sheet .
[102] P. Le Gargasson, M. Pelcat, N. Beuve, M. Pressigout, L. Morin, D. Menard, Pcbnco: A carbon intensity model of FR-4 printed circuit boards based on company data, in: 2025 IEEE Conference on Technologies for Sustainability (SusTech), IEEE, Los Angeles, CA, United States, 2025, http://dx.doi.org/10.1109/SusTech63138.2025.11025732 , URL https://hal.science/hal-05054490 .
[103] E.U. Enemuoh, V.G. Menta, A. Abutunis, S. O'Brien, L.I. Kaya, J. Rapinac, Energy and eco-impact evaluation of fused deposition modeling and injection molding of polylactic acid, Sustainability 13 (4) (2021) 1875, http://dx.doi.org/10.3390/su13041875 , Publisher: Multidisciplinary Digital Publishing Institute, URL https://www.mdpi.com/2071-1050/13/4/1875 .